The Pennsylvania State University

The Graduate School

Department of Materials Science and Engineering
Ceramic Science

$LaNiO_3$ BOTTOM ELECTRODES FOR FERROELECTRIC THIN FILMS

A Thesis in
Materials Science and Engineering

by
Zhenshan Zhang

Submitted in Partial Fulfillment
of the Requirements
for the Degree of

Master of Science

December 2000

Zhenshan Zhang

We approve the thesis of Zhenshan Zhang.

Date of Signature

12/9/2000

Susan Trolier-McKinstry
Associate Professor of Ceramic Science and Engineering
Thesis Advisor

12/08/00

Clive A. Randall
Professor of Materials Science and Engineering

12/08/00

Venkatraman Gopalan
Assistant Professor of Materials Science and Engineering

12/8/2000

Srinivas A. Tadigadapa
Associate Professor of Electrical Engineering

12/11/2000

Long-Qing Chen
Associate Professor of Materials Science and Engineering
Graduate Program Coordinator
of Materials Science and Engineering

Abstract

Ferroelectric thin films are being integrated into non-volatile memories, thin film capacitors, as well as pyroelectric and piezoelectric devices. In many of these applications, development of a preferred orientation state in the films leads to better homogeneity in the properties as the device size is reduced, and in some cases, superior properties. Thus, in this work, $LaNiO_3$ films were explored as orienting bottom electrodes for ferroelectric thin films in order to improve their piezoelectric coefficients. DC magnetron sputtering was used for deposition of the $LaNiO_3$.

$LaNiO_3$ powder was fabricated for preparation of three-inch sputtering targets using the molten salt technique. $LaNiO_3$ films were then grown on silicon and quartz substrates by DC magnetron sputtering. The influence of substrate temperature, gas ratio and working pressure on texture was studied and explained by adatom mobility and resputtering mechanisms. Optimal deposition parameters for highly (100)-textured $LaNiO_3$ films were determined.

The structure of the $LaNiO_3$ films was analyzed using X-ray diffraction. The full width at half maximum of the 200 reflections for the best (100)-oriented $LaNiO_3$ films from this work is 6.6°. The as-deposited lattice parameter of the $LaNiO_3$ thin films is 3.845 Å at room temperature. A thermal expansion coefficient of $16.3 \times 10^{-6}/^\circ C$ was determined for temperatures below 800°C. The temperature dependence of resistivity was characterized using a four-point probe. $LaNiO_3$ thin films exhibited typical metallic behavior, with a resistivity at room temperature of $8.0\times10^{-6}\ \Omega\cdot m$.

Strongly (100)-textured PbTiO$_3$, lead zirconate titanate (PZT) 52/48, and lead magnesium niobate-lead titanate (PMN-PT) 70/30 and 65/35 films were deposited on (100)-textured LaNiO$_3$/Si substrates by the sol-gel technique. The crystallization temperature for PMN-PT films on LaNiO$_3$ electrodes was reduced to 700°C, which is 50°C lower than that used on Pt electrodes. The resulting PMN-PT/LaNiO$_3$ films exhibited better dielectric and piezoelectric properties than the PMN-PT/Pt films. A remanent polarization of 12 μC/cm^2 was observed for (100)-oriented PMN-PT(70/30)/LaNiO$_3$ films annealed at 700°C. Effective piezoelectric coefficient d_{33} ~180 pC/N and d_{31} -79 pC/N were measured on a 1.1μm thick PMN-PT (70/30) film. Aging rates of 6.8%/decade and 3.9%/decade were observed for PMN-PT (70/30) films poled with the top electrode positive and negative, respectively.

(100)-oriented PMN-PT (70/30) films with LaNiO$_3$ bottom electrodes and Pt top electrodes exhibited very good endurance against cycling fatigue.

The influence of external stress was also investigated for PMN-PT (70/30) films. Samples under applied biaxial compressive or tensile stress exhibited different hysteresis loops at room temperature. The hysteresis loop rotated when external stress was applied to the PMN-PT films. With applied compressive stresses, the hysteresis loop rotated counterclockwise, resulting in an increase in the remanent polarization.

Table of Contents

List of Figures

List of Tables

Acknowledgements

I would like thank my advisor Dr. Susan Trolier-McKinstry for her guidance and support throughout this project. The education and motivation which I received from her will be beneficial for my whole life.

I would also like to thank The Office of Naval Research for providing the funding of this project.

My gratitude also go out to my colleagues and friends Dr. JeongHwan Park, Dr. Fei Xu, and Ron Polcawich. Thanks for their kind help in my research. It has been my pleasure to work with them.

My thanks are also extended to the faculty, support staff members and technicians in MRL for their kind assistance, especially William Drawl.

Finally, I need to acknowledge my parents and my wife. I couldn't finish my work without their support and understanding in the past years.

Chapter 1 Introduction and Goals of the Thesis

Much attention has been paid to ferroelectric thin films due to their potential use in dynamic random access memories, nonvolatile memories, decoupling capacitors and microelectromechanical systems [1]. In some cases, the electrical, ferroelectric and piezoelectric properties of the films have to be improved before they are widely used in ferroelectric integrated devices. Since most of the properties of ferroelectric films depend on their crystallographic orientation, highly oriented ferroelectric films are especially attractive and desirable for these applications [2]. In particular, many rhombohedral lead-based perovskite crystals oriented along their pseudocubic <001> direction exhibit large piezoelectric coefficients and good resistance to fatigue [3,4]. Through choosing appropriate electrodes and optimizing the processing parameters, highly (100)-oriented ferroelectric films can be deposited by many deposition techniques [5].

In order to obtain high performance devices, it is helpful to understand the behavior of both electrodes and thin films. Usually, ferroelectric thin films are grown on Pt-coated silicon wafers with Pt bottom electrodes. However Pt or Pt-based metal films are not ideal electrodes for some capacitors and are difficult to dry etch. The problems can include weak adhesion to the silicon substrates, a preference for (111) orientation, as well as unsatisfactory resistance to fatigue. To solve these problems and enhance the reliability, metallic oxides such as RuO_2, $SrRuO_3$, $La_{0.5}Sr_{0.5}CoO_3$ and $LaNiO_3$ can be used as electrodes [6-9]. Numerous reports have detailed growth of epitaxial metallic oxides on single crystal oxide substrates such as $SrTiO_3$, $LaAlO_3$ and MgO for bottom electrodes

[4,10]. Similarly, epitaxial growth of these materials can be achieved on Si, through the use of buffer layers such as TiN or MgO [11,12]. There are, however, numerous devices, including both MEMS (Microelectromechanical Systems) and memory elements where oriented films are needed on top of amorphous or polycrystalline layers. This can be achieved if the bottom electrode itself can be deposited fiber textured. Little information is available in the literature on routes to obtain textured metallic oxides on arbitrary flat surfaces. An exception is $LaNiO_3$, which tends to adopt (100) fiber texture on flat surfaces [9]. Since $LaNiO_3$ is a perovskite-structured metallic oxide down to 0.4 K [13], it can also be used as an oxide electrode with low lattice mismatch to many perovskite ferroelectric materials. Thus, it is possible to control the orientation of the ferroelectric films. Based on these advantages, $LaNiO_3$ thin films have attracted much attention as oxide electrodes.

Depositions of $LaNiO_3$ thin films have been reported by various techniques including pulsed laser ablation, spray combustion flame technique, rf magnetron sputtering, spray-ICP (inductive coupling plasma) and spin coating [14-18]. DC magnetron sputtering has not been used to deposit $LaNiO_3$ for electrodes. One of the objectives of this thesis is to fabricate strongly (001)-oriented $LaNiO_3$ electrodes on bare Si substrates using DC magnetron sputtering.

Towards this end, a molten salt technique was utilized to prepare 3-inch phase pure $LaNiO_3$ targets. Systematic investigations were then carried out to determine the optimal deposition conditions for highly (001)-oriented $LaNiO_3$ thin films. Specific attention was paid to the relations between processing parameters, orientation, and conduction behavior. In addition, temperature dependent structural analysis was used to determine the lattice parameter and thermal expansion coefficient.

Another goal of this thesis is to determine how the properties of ferroelectric films changed on using $LaNiO_3$ as bottom electrodes rather than Pt electrodes. To investigate this, the dielectric and piezoelectric properties were measured for (100)-oriented PMN-PT (70/30 and 65/35) thin films. To fully evaluate the properties of the PMN-PT films, the fatigue behavior, leakage current density and the field dependence of dielectric properties were also investigated on the PMN-PT thin films. To see the effect of $LaNiO_3$ electrodes, PMN-PT films with Pt and $LaNiO_3$ bottom electrodes were compared. Finally, the influence of residual stresses on the ferroelectric properties of PMN-PT thin films were analyzed by applying biaxial tensile and compressive stresses to the PMN-PT films.

Chapter 2 Literature Review

2.1 $LaNiO_3$

$LaNiO_3$ was chosen for the bottom electrode of {001} oriented ferroelectric films due to its combination of metallic conductivity and a good structural match with relaxor-$PbTiO_3$ perovskites. The difference of lattice parameters between the perovskite sub-cells of $LaNiO_3$ and relaxor-PT perovskites is less than 5% at room temperature.

2.1.1 Synthesis of $LaNiO_3$

Synthesis of $LaNiO_3$ was first carried out by Word, Post and Banks in 1957. They reacted nickel oxide with lanthanum oxide at 800°C to form a lanthanum nickel oxide with a perovskite-like structure. A sodium carbonate flux was used in the preparation to enable lower processing temperatures. Based on X-ray data, $LaNiO_3$ belongs to the space group D3d(5)-R3m with two formula units per unit cell. At room temperature, the dimensions of the rhombohedral cell are $a = 7.676$ Å and $\alpha = 90^{\circ}43'$ [19]. $LaNiO_3$ has a rhombohedrally distorted perovskite-type structure [19]. Throughout this thesis, the film orientation will be indexed in term of the simple cubic perovskite sub-cell.

The stability of $LaNiO_3$ in the perovskite structure is lower than for materials like $BaTiO_3$ or $SrTiO_3$. This can be justified in part on the basis of its position on the structure-field map. The tolerance factor of $LaNiO_3$ is 0.996 calculated from equation 2.1

using ionic radii suggested by Shannon [20-21]. A weighted average of the electronegativity difference of $LaNiO_3$ was calculated to be 1.98 by the equation $(X_{A\text{-}O} + X_{B\text{-}O})/2$ [22] using Pauling's electronegativity scale [23]. Since the electronegativity difference of $LaNiO_3$ is small and the tolerance factor is less than 1, $LaNiO_3$ is comparatively less stable and relatively difficult to synthesize as a perovskite [22].

$$t = \frac{r_A + r_O}{\sqrt{2}(r_B + r_O)} \qquad (2.1)$$

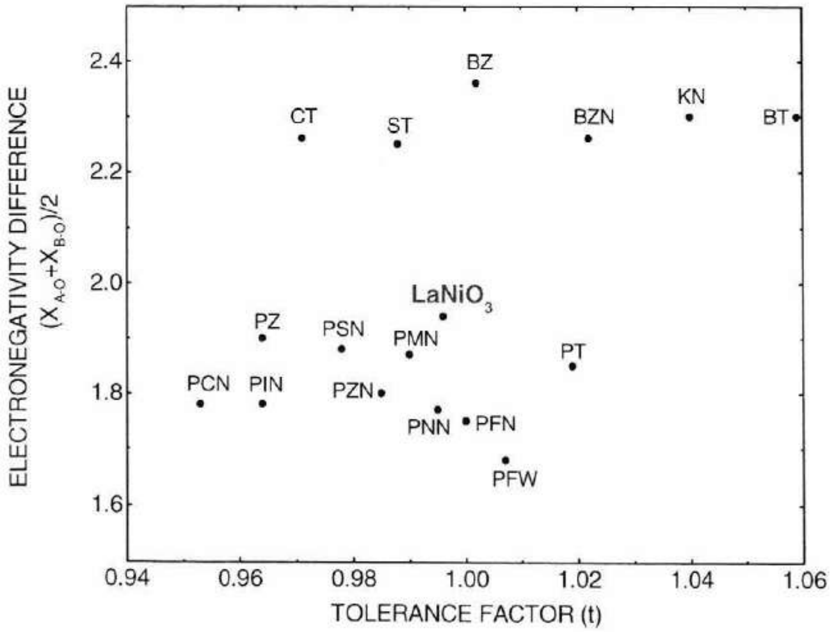

Fig. 2.1. Comparison of electronegativity difference versus tolerance factor between $LaNiO_3$ and other perovskite compounds [22].

The magnetic properties of $LaNiO_3$ were studied by neutron diffraction by Koehler and Wollan [24]. They found that there is no magnetic ordering for $LaNiO_3$ at temperatures down to 4.2 K. The magnetic and crystallographic properties of $LaNiO_3$ were investigated by Word *et al.* [25]. They suggested that Ni^{3+} ions in $LaNiO_3$ are in a low-spin state at room temperature that is compatible with the lattice symmetry and its Pauli paramagnetism.

The effect of temperature on the resistivity of ceramic $LaNiO_3$ was investigated by Obayashi [26]. As shown in Figure 2.2, $LaNiO_3$ exhibits typical metallic behavior and has a resistivity of $9.0 \times 10^{-5}\ \Omega\cdot m$ at room temperature.

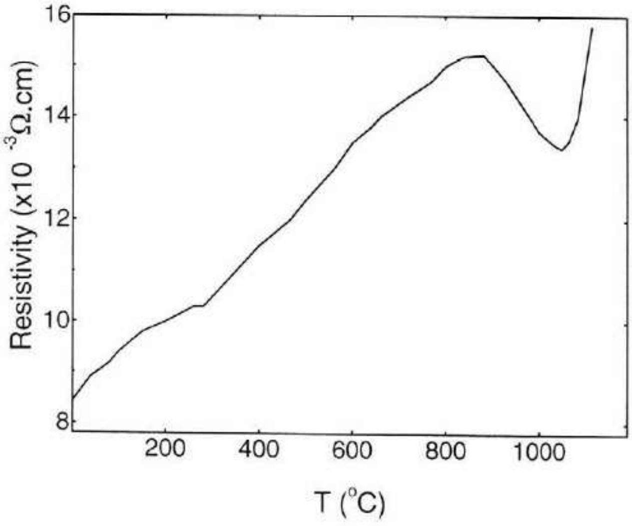

Figure 2.2. Resistivity of polycrystalline $LaNiO_3$ as a function of temperature [26].

2.1.2 Deposition of $LaNiO_3$ thin films

Its metallic conductivity and reasonable lattice match with other perovskite-type oxides such as $PbTiO_3$ and $YBa_2Cu_3O_{7-\delta}$ (YBCO) make $LaNiO_3$ a candidate for thin film electrodes. $LaNiO_3$ thin films have been fabricated by various techniques, including pulsed laser deposition, the spray combustion flame technique, rf magnetron sputtering, spray-ICP (inductive coupling plasma), and sol-gel routes [14-18].

Using pulsed laser deposition, epitaxial $LaNiO_3$ films have been grown on single crystal $LaAlO_3$, $SrTiO_3$, and yttrium-stabilized zirconia substrates by Satyalakshmi [14]. Deposition was carried out at substrate temperatures of 700°C under an oxygen partial pressure of 350 mtorr and the resultant $LaNiO_3$ films exhibited good metallic behavior. Sagoi *et al.* reported $LaNiO_3$ thin films obtained at 500°C exhibited Pauli paramagnetic properties and a low electrical resistivity of $1.5 \times 10^{-6}\ \Omega \cdot m$ at 15 K. In contrast, thin films obtained at 700°C showed a larger Curie-Weiss contribution to the magnetic susceptibility. The latter indicated the presence of local moments, probably associated with Ni^{II} species [27].

Using the spray-ICP technique, $LaNiO_3$ films were deposited on MgO, sintered high-purity alumina, Si or sapphire substrates at temperatures between 350 and 800°C at atmospheric pressure [17]. (111)- and (100)-oriented $LaNiO_3$ films were obtained on sapphire (001) and MgO (100) substrates, respectively. The resistivity of films deposited above 600°C was found to be $4.0 \times 10^{-6}\ \Omega \cdot m$.

Multilayer thin films of $BaTiO_3$-$LaNiO_3$ and $PbTiO_3$- $LaNiO_3$ have been deposited on MgO substrates using the spray combustion flame technique [15]. In similar studies, $LaNiO_3$ was deposited on sintered alumina, sapphire and MgO [28].

Radio frequency magnetron sputtering has also been used to deposit $LaNiO_3$ thin films on different substrates. Yang *et al.* reported that highly (100)-oriented $LaNiO_3$ thin films could be grown on Si, SiO_2/Si, Pt/SiO_2/Si and glass substrates at substrate temperatures from 150-500 °C. Films prepared at substrate temperatures of ~150-250 °C had a resistivity of $4\text{-}5 \times 10^{-6}\ \Omega\cdot$ m. These results indicated the strong tendency of $LaNiO_3$ films to adopt (100) texture on flat surfaces independent of the nature of the substrate Instead the orientation appears to be controlled by the deposition parameters [16].

2.1.3 Ferroelectric thin films on $LaNiO_3$ bottom electrodes

Yang *et al.* reported that sol-gel derived $Pb(Zr_{0.53}Ti_{0.47})O_3$ thin films on (100)-$LaNiO_3$/SiO_2/Si substrates had a significant level of {100} texturing [16]. As a result, ferroelectric capacitors fabricated from these films exhibited good polarization versus electrical field (P-E) hysteresis characteristics.

Using pulsed laser deposition, $(Pb_{0.97}La_{0.03})(Zr_{0.66}Ti_{0.34})O_3$ (PLZT) thin films were prepared on $LaNiO_3$/Si and $LaNiO_3$/Pt/Si substrates by Tseng *et al.* [29]. Highly (100)- and (110)-textured PLZT films were obtained on (100) and (110)-$LaNiO_3$ layers, respectively. The (100)-textured films exhibited remanent polarizations of 14.9 $\mu C/cm^2$, coercive fields of 3.5 kV/cm, dielectric constants of 950 and loss tangents less than 0.05 at 1 kHz.

2.1.4 Developing Orientation in Non-epitaxial Films

Epitaxy is a perfect three-dimensioned texture. This can be induced when there is a good crystallographic match between the film and the substrate. In many cases, however, there may not be such a convenient pairing. Preferred orientations are still possible, however, in this case, films have a preferred growth plane parallel to the substrate and random orientation with respect to rotation around the substrate normal. For phase pure growth, this orientation can be developed by kinetic routes, thermodynamic routes, or by resputtering. Kinetically-driven orientation is associated with the difference in deposition rates between different orientations. Thermodynamically-driven orientation requires a preferred facet and sufficient adatom mobility to minimize surface energy. This varies with materials and deposition parameters [30].

Movchan and Demchishin [31] proposed the structure zone model (SZM) to classify the grain structure of thin films according to the substrate temperature T during growth. The mobility of an adatom increases with temperature. At low temperature ($T/T_{melt} < 0.3$ i.e. zone I), films are amorphous or composed of fine grains due to low adatom mobility and atomic self-shadowing. At intermediate temperature ($0.3 < T/T_{melt} < 0.5$ i.e. zone II), films exhibit columnar grains which was attributed to the elimination of the effects of atomic self-shadowing by the high diffusion of adatoms [32]. At higher temperature

($T/T_{melt} > 0.5$), films exhibit equiaxed grain morphologies due to the dominant role of bulk diffusion. By introducing sputtering gas pressure to the SZM, Thornton [32] suggested that Zone T morphology in the low mobility range of $T/T_{melt} < 0.3$ with a low gas pressure (shown in Fig.2.3 [32]). Messier et al. suggested that the Zone T morphology was attributed to ion bombardment to the film surface during film growth. The ion bombardment was controlled by gas pressure [33].

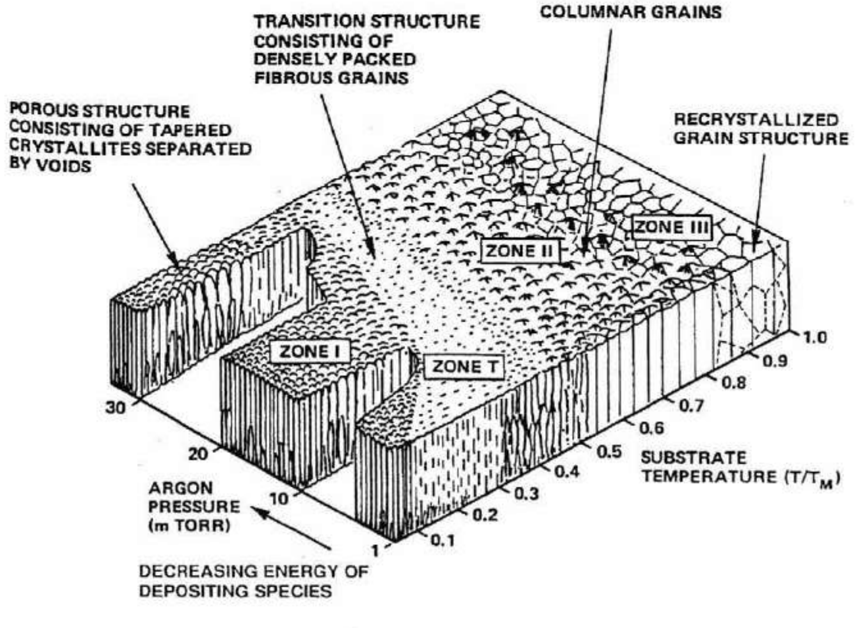

Fig. 2.3. Structure Zone Model (SZM) proposed by Thornton [32]

Selective evolutionary growth based on relative surface and interface energies is one mechanism for preferred orientation [34]. Orientation selectivity is created by crystallographic anisotropy in the film's free surface and interface energies. In order to minimize the surface energy, the adatoms with sufficient kinetic energy will occupy sites on the planes that have the lowest surface and interface energy density. So the grains with minimum surface and interface energy grow at higher rates than other grains. The minimization of surface and interface energy during the deposition will lead to crystallographic orientation. Thus, this selective occupation of the adatoms in thin films results in the development of preferred orientation.

Ion bombardment of the growing film during deposition can also result in preferred orientation [35]. When the resputtering mechanism is dominant, different sputtering yields for grains with various orientations lead to different growth rates. The growth of non-preferred grains is suppressed upon continued growth of the films and the close packed planes with higher growth rates will dominate the microstructure [35].

Resputtering can also affect the thickness and the microstructure of the growing film. Macro-effects change the overall thickness distribution of a film through a decrease in the growth rate. Micro-effects affect the surface morphology of a film at the μm-scale level. This was attributed to different resputtering yields for different average angles of incidence of the bombarding ions [36].

2.2 Ferroelectrics

2.2.1 Ferroelectricity

Ferroelectricity is a phenomena discovered in 1921. The major features of ferroelectricity include the ferroelectric hysteresis loop, ferroelectric domains and a spontaneous polarization. By definition, ferroelectricity is the ability to reorient a spontaneous electric dipole between equivalent crystallographic directions in a polar crystal by application of an electric field [37]. At temperatures above the Curie temperature (T_c), ferroelectricity disappears. As the material cools through T_c, ferroelectric materials experience a phase transformation from the paraelectric phase to a lower symmetry ferroelectric phase with a spontaneous polarization [37]. The dielectric constant reaches a maximum at T_c for most ferroelectric materials. The Curie-Weiss law (Equation 2.2) holds for many ferroelectric materials at temperatures above the Curie temperature:

$$K = C/(T-T_0) \qquad \text{(Equation 2.2)}$$

Where K is the dielectric constant, C is the Curie constant, T is the temperature, and T_0 is the Curie-Weiss temperature. T_0 is smaller than T_c for a first order ferroelectric material and equal to T_c for a second order ferroelectric phase transition.

Much attention has been focused on normal ferroelectrics including barium titanate ($BaTiO_3$), lead titanate ($PbTiO_3$), lead zirconate titanate (PZT), and relaxor ferroelectrics such as lead magnesium niobate (PMN). This led to their widespread use in areas such as dielectric ceramics for capacitor applications, piezoelectric materials for sensors, actuators and voltage transformers, pyroelectric detectors, ferroelectric thin films for non-volatile memories and electro-optic materials for data storage and displays [38].

Many of the commercially important ferroelectrics are based on the perovskite structure. The perovskites are a group of compounds with the general formula ABO_3. As shown in Figure 2.4 [37], in the ideal perovskite structure, the B cations sit at the center of the cell with the A cations on the corners and O anions in the face centers. This family also includes ferroelectrics with formula the $A(B'_x B''_{1-x})O_3$ in which the central atom is either B′or B″. On cooling through T_c, the cubic unit cell distorts into another structure (tetragonal, rhombohedral, orthorhombic, or monoclinic) in which the ions shift slightly in position to generate an electric dipole moment, and the crystal becomes spontaneously polarized [39].

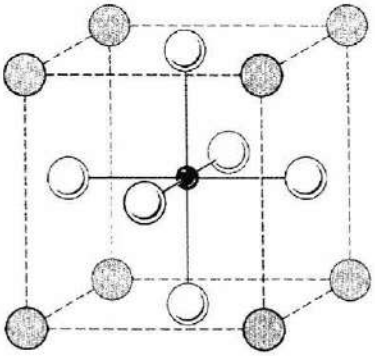

Figure 2.4. The perovskite unit cell from [35].

A major feature of ferroelectricity is the polarization electric field (P-E) hysteresis loop [40] (Fig. 2.5). OE is the saturation polarization that represents the total polarization attributable to ferroelectric switching. OD is the remanent polarization that represents the polarization remaining after the removal of the applied electric field. F is the coercive field [40]. The loop shows that there exists more than one possible crystallographic direction among which the spontaneous polarization can be switched by the applied electric field.

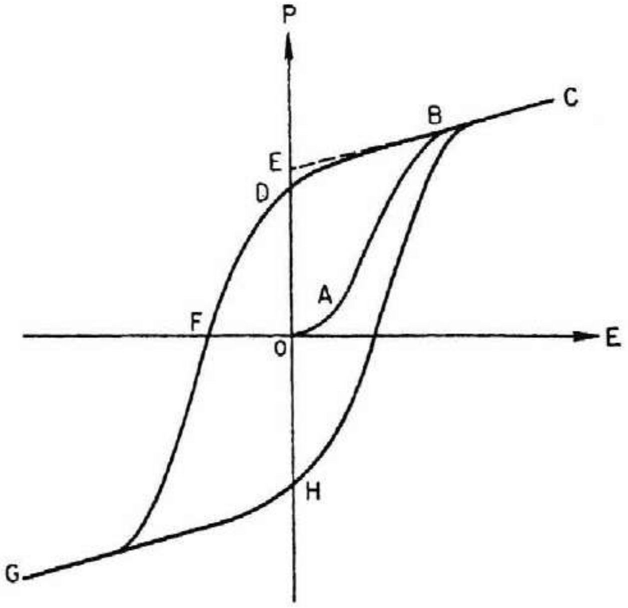

Fig. 2.5. Polarization electric-field (P-E) hysteresis loop, from [40].

2.2.2 Piezoelectricity

Piezoelectricity is a phenomenon discovered by the Curie brothers in 1880, in which electric charge on the sample surface is generated by an applied stress. The direct effect is the linear relationship between electric polarization and applied mechanical stress (Equation 2.3), and the converse one is the linear relationship between mechanical strain and electric field (Equation 2.4).

$$P_i = d_{ijk}\sigma_{jk} \qquad \text{(Equation 2.3)}$$

$$\varepsilon_{jk} = d'_{ijk}E_i \qquad \text{(Equation 2.4)}$$

Where P_i is the induced polarization, σ_{ij} is the applied stress, ε_{jk} is the field-induced strain, E_i is the applied electric field, and d_{ijk} in C/N and d'_{ijk} in m/V are piezoelectric coefficients. d_{ijk} and d'_{ijk} are numerically equivalent [41].

The absence of a center of symmetry is required in crystals to show the piezoelectric effect. Twenty of the 21 non-centrosymmetric point groups can demonstrate piezoelectricity. The only exception is point group 432 because the combination of all the symmetry elements eliminates piezoelectricity. Since all ferroelectrics belong to the ten polar point groups and these polar groups are a subset of the twenty piezoelectric point groups, all ferroelectric crystals are piezoelectric [42].

2.3 Relaxor Ferroelectrics

Relaxor ferroelectrics include a group of lead-based perovskite-type compounds with the general formula $Pb(B_1, B_2)O_3$ where B_1 is a lower valent cation (such as Mg^{2+}, Zn^{2+}, Ni^{2+}, and Fe^{3+}) and B_2 is a higher valent cation (such as Nb^{5+}, Ta^{5+}, W^{5+}) [40]. Relaxor ferroelectrics exhibit a broad diffused and dispersive phase transition on cooling below the Curie point that makes them different from normal ferroelectrics. The diffused phase transitions in relaxor ferroelectrics probably results from the compositional heterogeneity observed on a microscopic scale and breaks the translational symmetry of the lattice and the long range cooperation of dipole ordering [39]. As shown in Figure 2.6 [43], relaxor ferroelectric ceramics 0.9PMN-0.1PT and 0.87 $(Pb_{0.96}La_{0.02}\ K_{0.02})(Zn_{1/3}Nb_{2/3})O_3$-0.08 $PbTiO_3$-0.05 $BaTiO_3$ exhibit the temperature and frequency dependences of the dielectric constant that are common to all relaxor ferroelectrics. The main differences between relaxor and normal ferroelectrics are listed in Table 2.1 [44].

Table 2.1: Differences between normal and relaxor ferroelectrics [44].

Property	Normal Ferroelectric	Relaxor Ferroelectric
dielectric temperature dependence	sharp 1st or 2nd order transition at Curie point T_c	broad diffused phase transition at Curie maxima
dielectric frequency dependence	weak frequency dependence	strong frequency dependence
dielectric behavior in paraelectric range ($T > T_c$)	follows Curie - Weiss law	follows Curie - Weiss square law
scattering of light	strong anisotropy	very weak anisotropy to light
diffraction of X-rays	line splitting due to deformation from paraelectric to ferroelectric phase	no x-ray line splitting

In order to explain relaxor behavior, many models have been proposed, among which is the compositional inhomogeneity model suggested by Smolenskii [39]. He suggested that large fluctuations in the Curie temperature result from the fluctuations in the concentration of B_1 and B_2 cations observed on a microscopic scale and that there exists a mixture of polar and non-polar regions over a large temperature range. The primary experimental support for the compositional inhomogeneity model originated from investigations of the order-disorder behavior in $PbSc_{1/2}Ta_{1/2}O_3$ system [45-46].

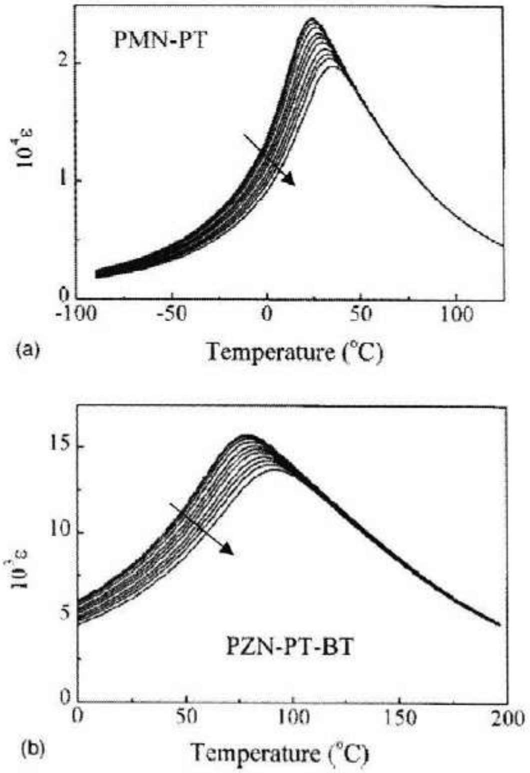

Fig. 2.6 Dielectric constant as a function of temperature at frequencies of 0.1, 0.12, 0.2, 0.4, 1, 2, 4, 10, 20, 40, and 100 kHz (increasing along arrows) for (a) PMN-PT and (b) PZN-PT-BT, from Cheng *et al.* [43]

Typical relaxor materials include $Pb(Mg_{1/3}Nb_{2/3})O_3$ (PMN), $PbZn_{1/3}Nb_{2/3}O_3$ (PZN), and $PbSc_{1/2}Nb_{1/2}O_3$ (PSN). They are attractive for various dielectric and MEMS applications due to their large dielectric permittivities and high electrostrictive strains. Through the addition of ferroelectric $PbTiO_3$ (PT), the solid solutions of PMN-PT, PZN-PT and PSN-PT can be formed. These solutions have a morphotrophic phase boundary (MPB) between rhombohedral and tetragonal phases, which are at about 0.33-0.34 PT in PMN-PT solutions, at about 0.095 PT in PZN-PT solutions and at about 0.42-0.43 PT in PSN-PT solutions [47-49]. Single crystals near the MPB composition demonstrate maximum values of the piezoelectric coefficient along the <001> direction [3]. The phase diagram of PMN-PT (which is of interest for this thesis) is shown in Figure 2.7 [50].

The piezoelectric properties of single crystal $Pb(Zn_{1/3}Nb_{2/3})O_3$–$PbTiO_3$ (PZN-PT) were investigated by Park *et al.* [3]. As shown in Fig. 2.8, d_{33} increased with increased amount of $PbTiO_3$ for <001>-oriented rhombohedral crystals. Although <111> is the polar direction for rhombohedral crystals, such cuts exhibited lower piezoelectric coefficients. The anisotropy in d_{33} probably originates in part, from a rhombohedral-tetragonal phase transition induced by an electric field applied along the <001> direction [3]. Because of the electric field, the polar direction inclines towards the direction of the electric field in all domains and increases the distortion of the unit cell. As the electric field increases, the polarizations ultimately switch to <001>, resulting in the rhombohedral-tetragonal phase transition. Their results implied that <001> oriented rhombohedrally-distorted perovskite films have the potential for enhanced piezoelectric response relative to random or <111> oriented films.

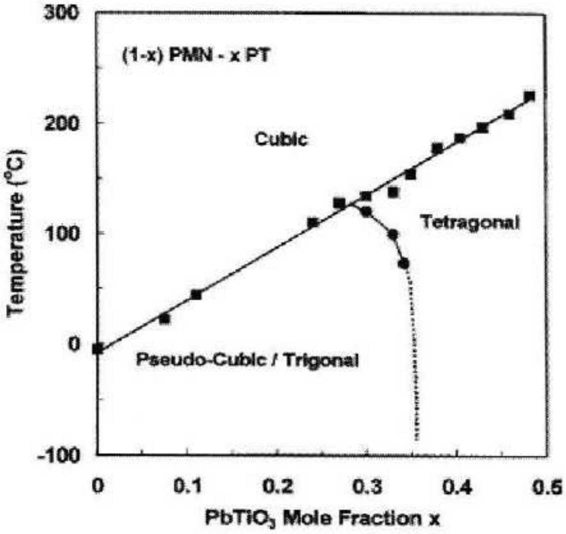

Fig. 2.7. Phase diagram of lead magnesium niobate titanate, from Choi *et al.* [50].

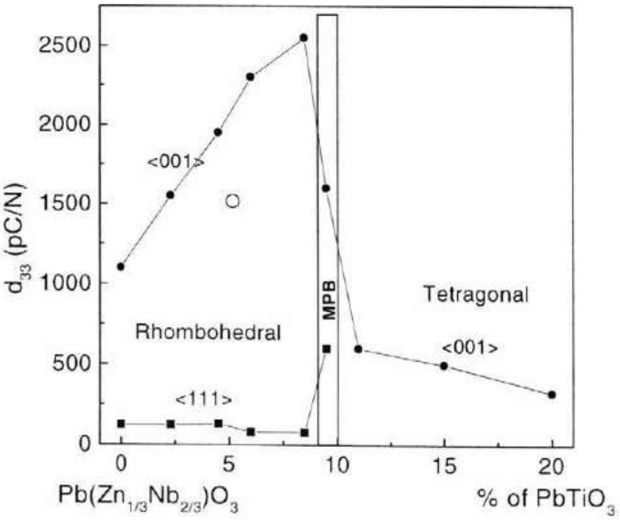

Fig. 2.8. d_{33} as a function of crystal composition and orientation for PZN-PT, from Park *et al.* [3].

2.4 Relaxor-PT Thin Films

Relaxor–$PbTiO_3$ thin films have been prepared by radio frequency (rf) sputtering, metalorganic chemical vapor deposition, pulsed laser deposition, and sol-gel techniques on different substrates. Due to the anisotropy of ferroelectric crystals, all the properties strongly depend on the crystallographic orientation. The orientations of thin films are strongly affected by the bottom electrodes utilized.

Radio frequency magnetron sputtering was used in preparation of $Pb[(Mg_{1/3}Nb_{2/3})_{0.7}Ti_{0.3}]O_3$ thin films on $Pt/Ti/SiO_2/Si$ substrates with PbO-enriched targets by Jiang *et al.* in 1994 [51]. The ferroelectric films deposited at 640°C have a room temperature dielectric constant greater than 2000.

Metalorganic chemical vapor deposition (MOCVD) was used to prepare $Pb(Mg_{1/3}Nb_{2/3})O3–PbTiO_3$ thin films by Takeshima *et al.* in 1995 [52]. (100)-oriented MgO single crystals with Pt(100) electrodes and (100)-Si wafers with $Pt(111)/Ti/SiO_2$ layers were used as substrates to deposit $Pb(Mg_{1/3}Nb_{2/3})O3–PbTiO_3$ thin films with compositions of Ti/(Mg+Nb+Ti) >25 mol% at 680-780°C. The resultant PMN-PT thin films exhibited (100) orientation and a dielectric constant of 1000-1500 at room temperature.

Recently, epitaxial $Pb(Mg_{1/3}Nb_{2/3})O_3$ (PMN) thin films were deposited on (001) $SrTiO_3$ and $SrRuO_3/SrTiO_3$ substrates using MOCVD by Bai *et al.* [53]. For a 200-nm-thick PMN film deposited on $SrRuO_3/SrTiO_3$ at 700°C, the zero-bias dielectric constant and loss measured at room temperature and 10 kHz were approximately 1100 and 2%, respectively. The remnant polarization for this film was 16 $\mu C/cm^2$. Stemmer *et al.* [54] reported that epitaxial (1-x) $Pb(Mg_{1/3}Nb_{2/3})O_3$–x $PbTiO_3$ (x = ~ 0.15-0.3) thin films were also prepared on (100) $SrTiO_3$ substrates at 725-735°C using MOCVD. The perovskite films were pyrochlore free and contained a Mg-rich impurity phase when magnesium-rich growth conditions were used.

Pulsed laser deposition can also be used to deposit relaxor-$PbTiO_3$ thin films. Tyunina *et al.* reported that highly (100)-oriented films of $PbMg_{1/3}Nb_{2/3}O_3$–$PbTiO_3$ and $PbSc_{1/2}Nb_{1/2}O_3$ –$PbTiO_3$ with compositions near the morphotropic phase boundary were prepared by pulsed laser deposition on $La_{0.5}Sr_{0.5}CoO_3$/MgO (100) [55]. The films exhibited polarizations and dielectric permitivities close to those in the corresponding bulk ceramics at room temperature and relaxor behavior, with broader transitions in the films larger than in bulk ceramics.

Using pulsed laser deposition, Maria *et al.* deposited (001)-oriented epitaxial $0.7Pb(Mg_{1/3}Nb_{2/3})O_3$–$0.3PbTiO_3$ thin films on $LaAlO_3$ substrates with $SrRuO_3$ bottom electrodes. The films exhibited room temperature dielectric constants greater than 1500, d_{31} piezoelectric coefficients of up to −180 pC/N, well developed Curie–Weiss behavior, and remanent polarizations of 13-20 $\mu C/cm^2$ [56].

The sol-gel spin-on technique was used to fabricate lead magnesium niobate-lead titanate thin films with the morphotropic phase boundary composition on Pt/Ti/SiO_2/Si substrates by Udayakumar *et al* [57]. The rapid thermally annealed films showed a high dielectric constant of 2900 and low dissipation factor of 0.02 with a remanent polarization of 11 $\mu C/cm^2$ and coercive voltage of 11 kV/cm.

Using a modified sol-gel process, Park *et al.* deposited polycrystalline $0.7Pb(Mg_{1/3}Nb_{2/3})O_3$-$0.3PbTiO_3$ thin films with (111) and (100) orientations on Pt(111)/Ti/SiO_2/Si substrates. The room temperature dielectric constant was 2500-2600 for the (100)-oriented and was 1900-2000 for (111)-oriented films. The (100)-oriented PMN-PT films exhibited larger piezoelectric coefficients than (111)-oriented films. The d_{33} coefficients of the 1.5 μm thick (100)-oriented PMN-PT films were 170-183 pC/N [58].

They concluded that (100)-oriented PMN-PT thin films could be deposited on Pt(111)/Ti/SiO_2/Si substrates and demonstrated better dielectric and piezoelectric properties than (111)-oriented thin films. Strongly (100)-oriented PMN-PT thin films are expected to grow on (100)-oriented $LaNiO_3$ bottom electrodes.

2.5 PZT thin films

An alternative to the relaxor-PT systems as thin film actuators is lead zirconate titanate ($Pb(Zr_xTi_{1-x})O_3$, PZT). PZT is a solid solution whose end members are orthorhombic antiferroelectric $PbZrO_3$ and tetragonal ferroelectric $PbTiO_3$. PZT has a perovskite type structure with the Ti^{4+} and Zr^{4+} ions occupying the B site randomly. PZT is a paraelectric with the cubic perovskite structure above the Curie point and ferroelectric with tetragonal or rhombohedral structures below the Curie points over the most of the phase diagram. The spontaneous polarization is along $<001>_c$ in the tetragonal phase and along $<111>_c$ in the rhombohedral phase [57]. (where c denotes the direction with respect to the cubic prototype cell).

As shown in the PZT phase diagram (Fig. 2.9), the morphotrophic phase boundary (MPB) with a room temperature composition $Pb(Zr_{0.52}Ti_{0.48})O_3$ separates the ferroelectric tetragonal and rhombohedral phases. PZT with the MPB composition has excellent piezoelectric properties. The poling of PZT is easy at this composition due to existence of 14 possible orientations for the spontaneous polarization including eight $<111>_c$ directions in the rhombohedral phase and six $<001>_c$ directions in the tetragonal phase [59].

2.6 Stresses in Thin Films

Residual stresses have a significant effect on thin film properties. In order to improve the properties of thin films in electronic devices, it is necessary to study residual stress and its effects. The residual stresses originate from growth strains and thermal strains due to the thermal expansion mismatch between film and substrate [60]. Stresses in the films vary with growth conditions even using the same film deposition technique [61].

The effects of biaxial and uniaxial stresses have been studied for PZT films [62-65]. Shepard *et al.* investigated the effects of tensile and compressive biaxial stresses on the properties of sol-gel derived PZT thin films [66]. According to his research, the change of dielectric constant is reversible and less than 5% under 100 MPa. Remanent polarizations decrease under tensile stress and increase under compressive stress.

Changes in the remanent polarization are reversible and less than 25% under 100 MPa. He concluded that ferroelastic wall motion is strongly constrained in PZT films and little stress response results from non-180° domain wall motion.

The effects of uniaxial and biaxial stresses on the properties of PMN-PT films have not been reported. This kind of experiment is very helpful for understanding the stress behavior and improving the properties of PMN-PT thin films.

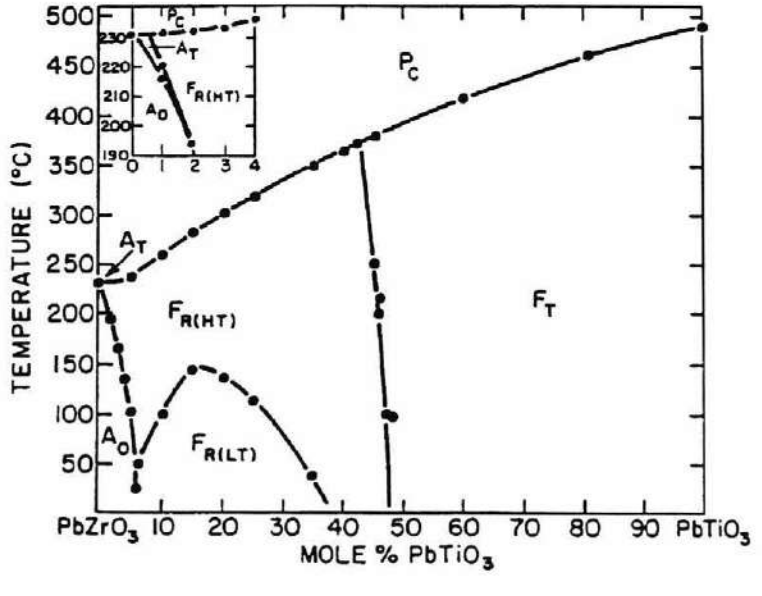

Fig. 2.9 The lead zirconate titanate phase diagram. P_c is the paraelectric cubic phase, F_T is the ferroelectric tetragonal phase, $F_{R(HT)}$ is the high temperature ferroelectric rhombohedral phase, $F_{R(LT)}$ is the low temperature ferroelectric rhombohedral phase, A_O is the antiferroelectric orthorhombic phase, and A_T is the antiferroelectric tetragonal phase, from Jaffe *et al.* [59].

Chapter 3 Experimental Procedure

3.1 Description of DC Magnetron Sputtering System

Since $LaNiO_3$ is a metallic oxide, it can be deposited using DC magnetron sputtering. The following is a brief description of the system used for growth.

Fig. 3.1 gives a schematic of DC magnetron sputtering system. The mechanical pump (CIT-ALCATEL ZT2033C) and the chamber are connected by a roughing line with a roughing valve to open and close it. The diffusion pump (Varian) is connected to the mechanical pump and chamber by the backing line and gate valve respectively. Three 3-inch target holders are built into the chamber door. The sputtering power is supplied by magnetron drives (MD-1K, Advanced Energy Industries, Colorado), and the chamber pressure is measured by an ionization gauge (Granville-Phillips). Clean nitrogen gas (98%) is used to vent the chamber.

3.1.1 System Operation

In order to prevent diffusion pump oil from backstreaming into the chamber, the roughing and backing valves should not be open at the same time. To avoid oxidation of the diffusion pump oil, a working diffusion pump cannot be open to air at any time. Therefore the chamber must be pumped down to 50 mtorr before it is opened to the working diffusion pump. Before the diffusion pump is turned on, the gate valve was closed and the backing valve opened to let the mechanical pump backup the diffusion pump. Meanwhile, the cooling water was turned on. After the diffusion pump was turned off, the mechanical pump was used to backup the diffusion pump for at least 20 minutes.

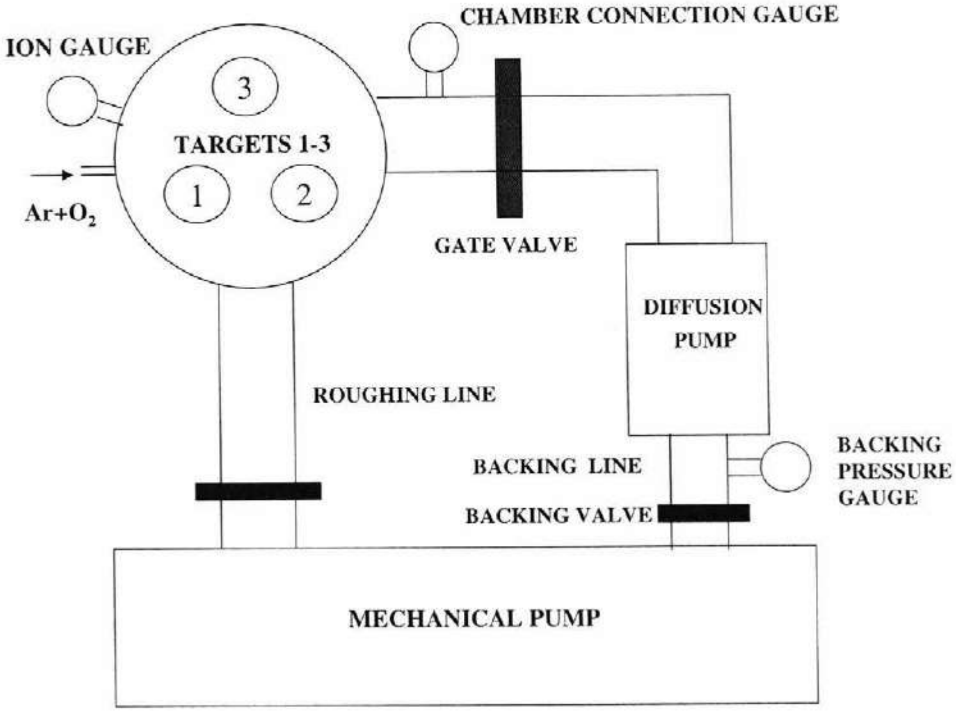

Fig. 3.1 Schematic of DC magnetron sputtering system

As shown in Fig. 3.2, a sample holder placed opposite the target was heated by 3 heating elements (Tempco HD04-0108B, Wood Dale, IL). Substrates are attached on the sample holder with silver paint which was heated in an oven at 150 °C for 15 minutes to remove the solvent in the silver paint. When the chamber pressure was pumped down to

~ 2×10^{-6} torr, the substrates were heated to 500°C and various mixtures of Ar and O_2 were then introduced into the chamber to maintain a working pressure of ~50 mtorr. Since a clean target and process gas help to obtain high purity films, the target was presputtered for five minutes to clean the surface before films were deposited. The shutter was then removed from the target so that films could be deposited onto substrates. Usually depositions were carried on for 1 to 3 hours.

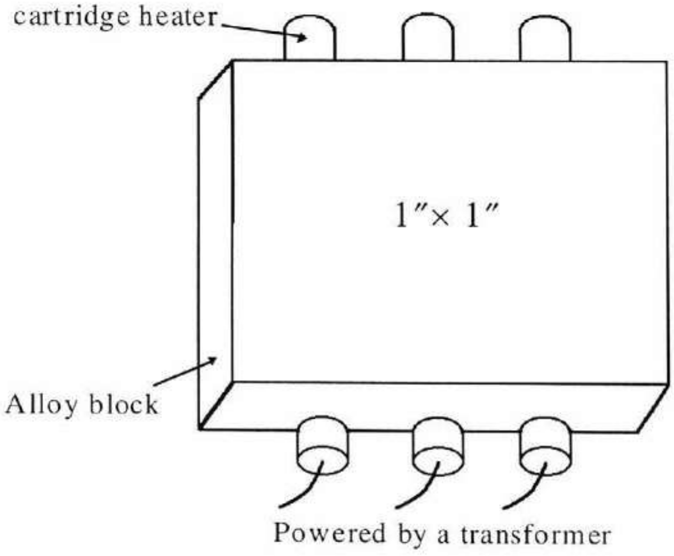

Fig. 3.2 Schematic of the substrate heater

3.2 $LaNiO_3$ Target Fabrication

The $LaNiO_3$ powder was prepared using a molten salt technique with Na_2CO_3 as a flux [22]. As shown in Fig. 3.3, a stoichiometric mixture of NiO and La_2O_3 together with an equal weight of Na_2CO_3 were heated at 850°C for 30 hours, and then cooled to room temperature. To wash away the flux, the powder was put into a 500ml beaker with de-ionized water. Then it was stirred and heated on a hot plate to 100°C to solvate the Na_2CO_3. Shortly after stirring was stopped, the remaining powder sedimented, and the upper clear solution was poured out. This procedure was repeated ten times until no sodium ions were detected in the solute using a flame test.

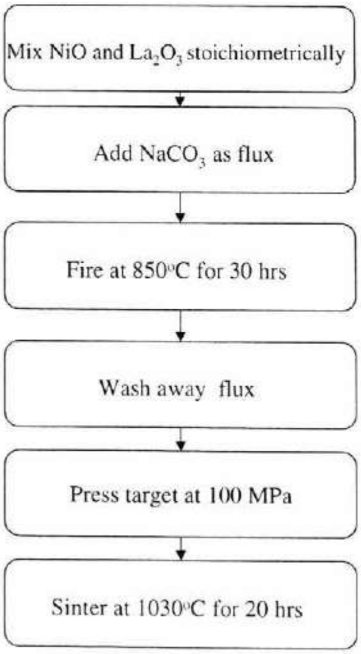

Fig. 3.3 Flow chart of $LaNiO_3$ target processing

$LaNiO_3$ powder with 3 weight % acryloid resin as binder was then pressed in a die at a hydrostatic pressure of ~100 MPa. The compact was then heated slowly at a rate of 2°C/min and held at 550°C for 5 hours to let the binder burn out completely. Then it was sintered at 1030°C for 20 hours in an open-air atmosphere and was finally cooled down slowly in a furnace. It was found that the target was phase-pure $LaNiO_3$ by XRD (shown in Fig. 3.4).

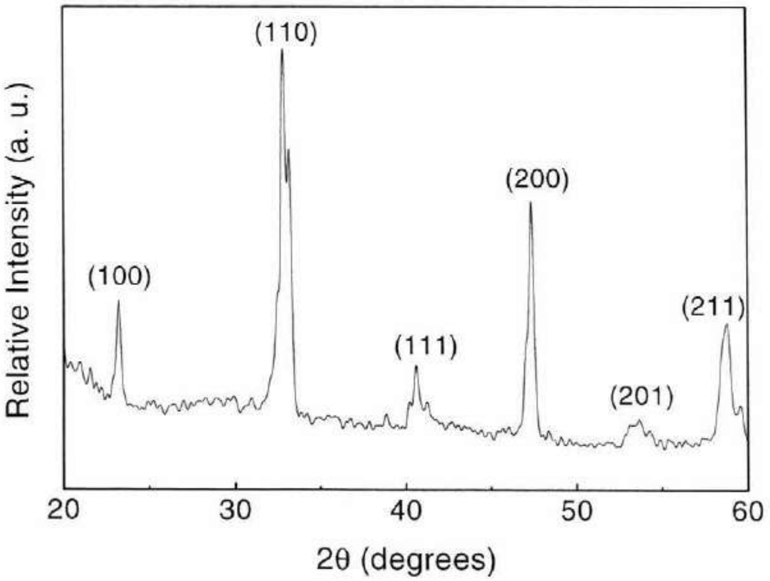

Fig. 3.4 XRD pattern of $LaNiO_3$ target

3.3 Deposition of $LaNiO_3$

The bare silicon and glass substrates were cleaned using acetone and were then mounted on the sample holder using silver paint. The sample holder with the sample was heated in a box oven (Antek 3000) at 150 °C for 15 minutes to eliminate the solvent in the silver paint. The target holder was then mounted in the chamber and the system was pumped to a base pressure of $\leq 2\times 10^{-6}$ torr. A mixture of high purity O_2 and Ar was used to deposit $LaNiO_3$ thin films. The distance and angle between target and substrate are 11cm and 35°, respectively. In order to obtain textured $LaNiO_3$ thin films, working gas pressures of 20-60 mtorr, substrate temperatures of 300-700°C and gas ratios between O_2 and Ar of 30-70% were investigated in this work. The power used for depositions was 200W. The growth rate was calculated from the thickness and deposition time.

3.4 Deposition of Ferroelectric Thin Films

The sol-gel technique was used in this work to deposit ferroelectric thin films because of its ease in controlling composition. In the first step, precursors are reacted in an organic solvent to obtain a proper stoichiometry. In the second step, substrates are spin coated with the solution and heated on a hot plate at low temperature for several minutes to remove organic solvent. Then they are annealed at high temperature in a rapid thermal annealer (RTA, Heatpulse 610, A.G. Associates, San Jose, CA) for the film to crystallize.

To prepare PZT(52/48) solutions, lead acetate trihydrate ($Pb(CH_3COO)_2\cdot 3H_2O$), zirconium n-propoxide ($Zr[OCH(CH_3)_2]_4$) and titanium isopropoxide ($Ti[OCH(CH_3)_2]_4$) were used as starting materials [67]. The lead acetate trihydrate was solvated in a 2-methoxyethanol solvent and the solution was refluxed for 2 hours and dehydrated at 110°C under a vacuum of 130mbar in a rotary evaporator. Then the mixed solution of zirconium n-propoxide and titanium isopropoxide in 2-methoxyethanol was refluxed with the lead acetate solution at 120°C for 2 hours. The final solution is adjusted to 0.4 Molar with 12% excess lead and 4vol% formamide to prevent cracking during subsequent thermal treatment. To deposit PZT films, the PZT solution was spin coated onto the substrate at 1500 rpm for 30 seconds. Then each PZT layer was pyrolyzed at 360°C for 120 seconds on a hot plate and crystallized at 700°C for 30 seconds in an RTA. The resulting thickness per layer was ~ 0.08 μm. Crystallization was performed after each spin-coat to force nucleation at the film-"substrate" interface, so that the bottom electrode could control the final film orientation.

To prepare the PMN-PT (70/30 and 65/35) solutions, lead acetate trihydrate ($Pb(C_2H_3O_2)_2 \cdot 3H_2O$), magnesium ethoxide ($Mg(OC_2H_5)_2$), niobium ethoxide ($Nb(OC_2H_5)_5$) and titanium isopropoxide ($Ti(OCH(CH_3)_2)_4$) (Aldrich Chemical, Milwaukee,WI) were used as starting materials. The procedure followed was given by Park *et al.* [68]. The magnesium ethoxide and niobium ethoxide were mixed in a 2-methoxyethanol solvent and refluxed at 120°C under a dry nitrogen gas flow for 24 hours. Then titanium isopropoxide was added and the solution was refluxed under flowing dry nitrogen gas for 6 hours to get a Mg/Ni/Ti complex solution. The lead acetate trihydrate solution was refluxed at 120°C for 3 hours and then distilled to eliminate water. Finally, the lead solution was added into the complex solution and the solution was refluxed at 120°C in dry nitrogen gas flow for another 5 hours. The final solution was adjusted to 0.5M, and 4vol% formamide was added. The solution processing is shown in Fig. 3.5 [68]. To deposit PMN-PT films, the solution was spin coated onto substrates at

7500 rpm for 30 seconds for each layer. Then the PMN-PT layer was pyrolyzed at 360°C for 150 seconds on a hot plate and crystallized between 600 and 800°C for 60 seconds in an RTA for each layer. The resulting thickness per layer was ~ 0.09 μm.

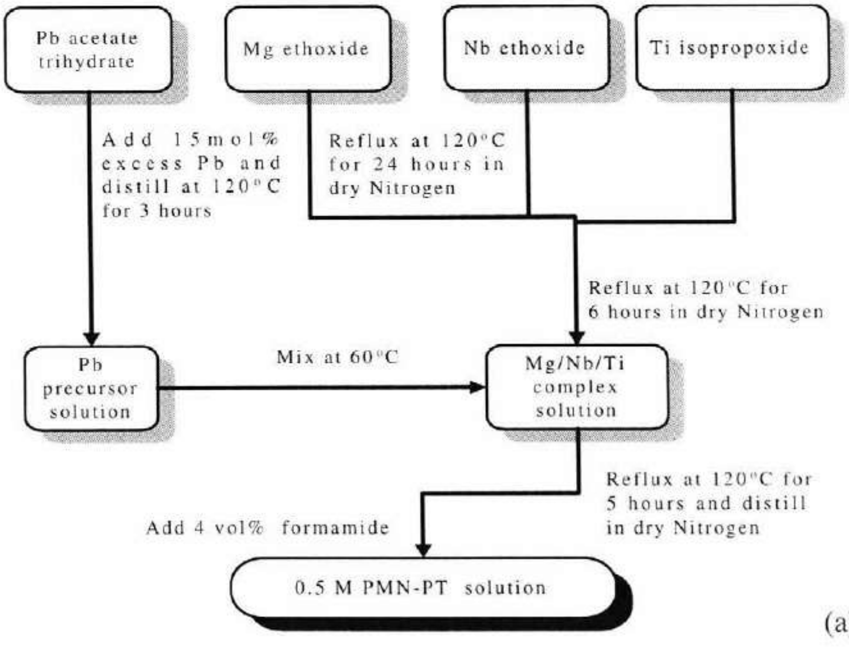

Fig. 3.5 (a) Flow chart of the sol-gel technique for the preparation of PMN-PT solutions, from Park *et al.* [68]

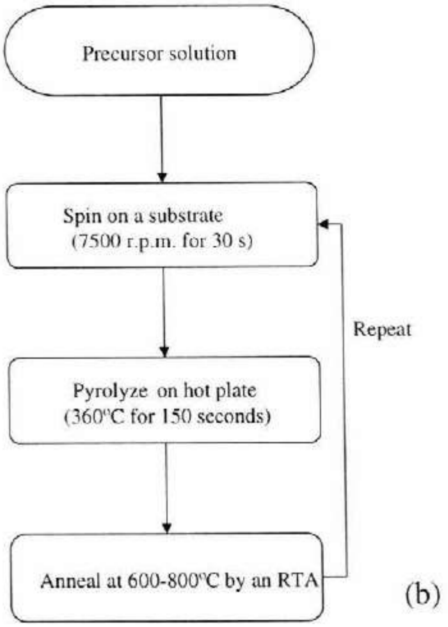

Fig. 3.5 (b) Flow chart of the sol-gel technique for the preparation of PMN-PT thin films

3.5 Structure Characterization

3.5.1 X-ray Diffraction

To determine the phase and the orientation of both powder samples and films, x-ray diffraction patterns were recorded using a Scintag DMC-105 diffractometer with Cu Kα radiation at room temperature. The 2θ sweep was from 20° to 60° at a rate of 4 degrees/min in a θ-2θ continuous scan.

According to the equation 3.1 from Chu *et al.* [69], The degree of orientation for the $LaNiO_3$ films was calculated using the normalized data with respect to randomly textured $LaNiO_3$.

$$[(I/I^*)_{100}+(I/I^*)_{200}]/[(I/I^*)_{100}+(I/I^*)_{110}+(I/I^*)_{200}+(I/I^*)_{111}] \qquad \text{(equation 3.1)}$$

Where I and I^* are the integrated intensities of the (100), (110), (111) and (200) peaks of $LaNiO_3$ film and of $LaNiO_3$ bulk ceramic powder.

Since strong (100)-orientation of $LaNiO_3$ films is preferred, it is necessary to examine the texture of $LaNiO_3$. The rocking curve of the 200 peak was measured on sweeping ω from 2° to 50° using a step size of 0.02° and a scan rate of 0.04°/min. Full width at half maxima (FWHM) were calculated for $LaNiO_3$ films deposited at different conditions.

In order to determine the lattice parameter and thermal expansion coefficient of the $LaNiO_3$, a 2-circle x-ray diffractometer with a radiant furnace was used to record the x-ray diffraction patterns from room temperature to 1000°C. The sample was maintained at each measurement temperature for five minutes before starting a scan to improve the accuracy of the measured lattice constant. A step scan was performed using a step of 0.02° and step scan rate of 0.04 degrees/min. A standard Si powder was used for angle calibrations in this work. The Si peak at $2\theta = 28.447°$ was used for a standard. The lattice parameter of Si at different temperatures was calculated using the thermal expansion coefficient of Si ($\alpha_{Si} = 3.8\times10^{-6}/°C$) [66]. The angle shifts of Si peaks were calculated using Bragg's law $n\lambda=2d\sin\theta$ ($\lambda_{Cuk\alpha}=1.5418$ Å). The corrected angles for the $LaNiO_3$ 100 peak were then calculated according to the corresponding shift of Si ($2\theta < 0.02^{\circ}$). Lattice constants a_{pc} were then calculated from the real angles for the $LaNiO_3$ 100 peak. The thermal expansion coefficient was finally calculated from the plot of a_{pc} versus temperature.

3.5.2 Film Topography and Thickness

In this study, atomic force microscopy (Multi-mode AFM, Digital Instruments) and scanning electron microscopy (Hitachi S-3500N) were used to examine the microstructure of $LaNiO_3$, PZT and PMN-PT thin films. An Alpha-Step 500 surface profilometer (Tencor Instruments, Mountain View, CA) was used to measure the thickness of the film with a step. A HCl solution (30vol%HCl: 70vol%H_2O: 5vol%HF) was used to etch steps in the $LaNiO_3$ films. Two ways were used to obtain a step for ferroelectric films. First involved etching the ferroelectric films using a HCl solution to expose the bottom electrode underneath. The other way was to cover a corner of the substrate with a tape during the spin coating for each layer and remove it during the subsequent pyrolysis and annealing. Since the HCl solution can also etch $LaNiO_3$ easily, the second method was used to measure the thickness of ferroelectric films deposited onto $LaNiO_3$ electrodes.

3.6 Electrical Property Measurements

For electrical characterization of the ferroelectric thin film, the $LaNiO_3$ layer (~600 Å thick) and a Pt (~ 600 Å thick) layer were used as the bottom and top electrodes respectively. The Pt layer was deposited onto the ferroelectric film using sputtering and the sample was then annealed at 350°C-700 °C for 2 minutes. The dielectric constant and loss tangent of ferroelectric films were measured at 1 kHz and 30 mV using an impedance analyzer (Hewlett Packard 4192A). The fatigue behavior and polarization-electric field hysteresis loop of the films were measured by a RT66A ferroelectric test system (Radiant Technology, Albuquerque, NM). The leakage current was measured using a pA meter (Hewlett Packard 4140) for electric fields from 0 to 110kV/cm with a delay time of 5 seconds for each electric field.

In order to measure the temperature dependence of resistivity, $LaNiO_3$ thin films coated on glass substrates were heated from room temperature to 350°C in an oven (Eurotherm, EUR 808). Electrical connections were made between the sample and a 4-point probe test fixture using silver epoxy contacts. The 4-point set-up eliminates the contribution from contact resistance. A current of 20 mA was applied by a DC power supply (Hewlett Packard, E3612A) through the outer two probes; the voltage across the inner two probes was measured using a multimeter (Hewlett Packard, 3478A) to determine the film resistivity.

In order to measure the effect of biaxial stresses on the polarization-electric field hysteresis loop for PMN-PT/$LaNiO_3$/Si, tensile stresses were applied to samples using the wafer and O-ring configuration shown in Fig. 3.6 [66] and compressive stresses were applied to samples using the chip-on-steel configuration shown in Fig. 3.7 [66]. In chip-on-steel measurements, a 3"steel plate was deformed into a dome by the gas pressure in the rig and a PMN-PT chip was then glued onto the top of the dome. Then the electrical leads and strain gauge (Omega KFG-an-120-C1-11L3M3R) were attached to the PMN-PT chip and the steel-chip side was placed facing down before the gas was introduced into the cavity.

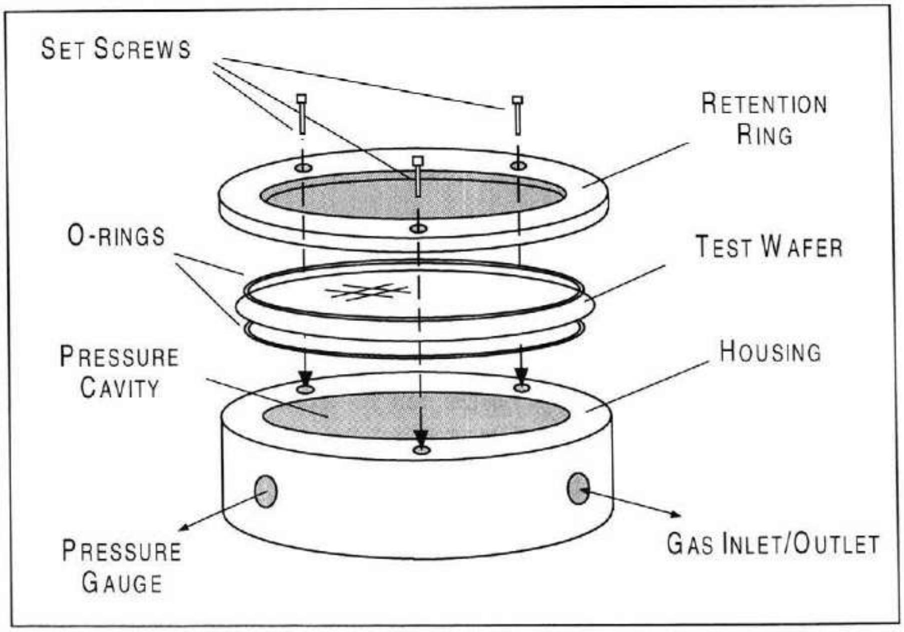

Fig. 3.6 The wafer and O-ring configuration for application of tensile stresses on PMN-PT films, from Shepard [66].

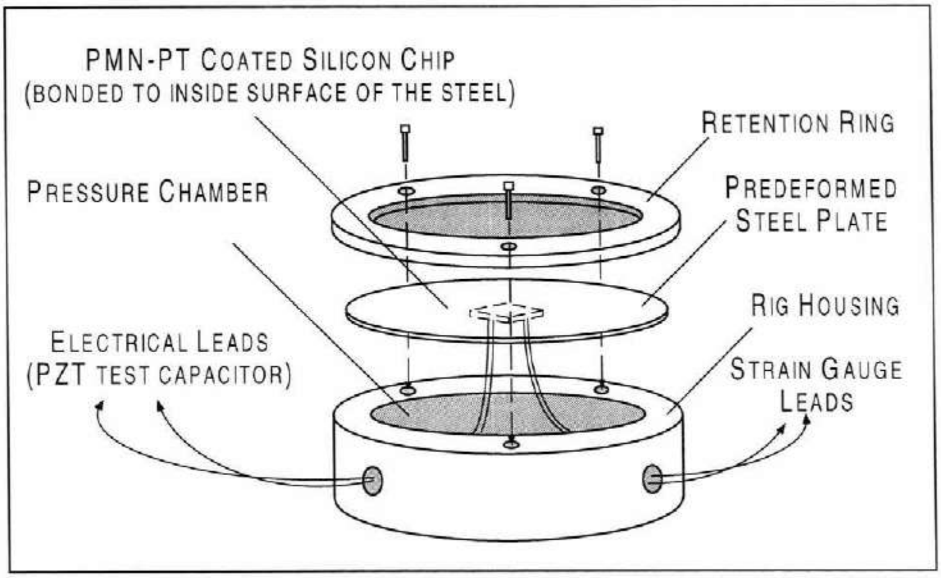

Fig. 3.7 The chip-on-steel design for application of compressive stresses applied on PMN-PT films, from Shepard [66].

3.7 Piezoelectric Property Measurements

The piezoelectric coefficient d_{31} of the films was measured using the wafer flexure technique developed by Shepard and Maria *et al.* [66,71]. Fig. 3.8 shows a schematic of the wafer flexure apparatus [71]. The d_{31} coefficient can be determined from measuring the strain and charge induced by flexing the wafer periodically. To calibrate the apparatus, two PZT coated Si chips with known piezoelectric coefficients were used for strain and charge calibration under the same oscillation conditions.

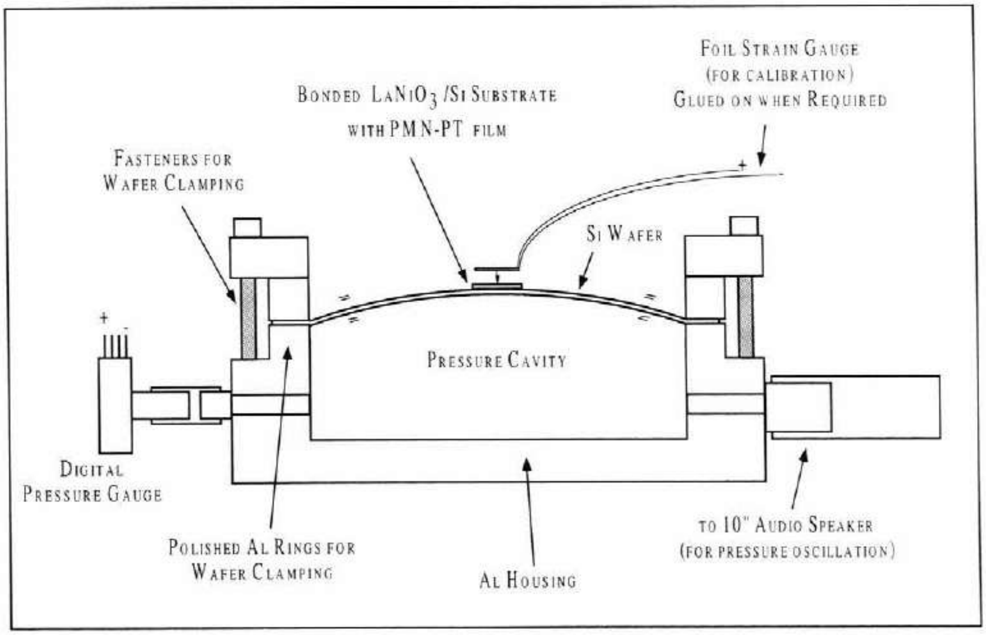

Fig. 3.8 Schematic of modified wafer flexure apparatus from Maria [71].

The piezoelectric coefficient d_{33} of the films was measured using the pneumatic pressure charge method developed by Xu *et al.* [72]. The experimental setup of the technique is shown in Fig. 3.9 [72]. Both double beam interferometry and the Berlincourt method were used to calibrate the pneumatic pressure charge technique. The backs of samples were polished and the O-ring was lubricated to minimize the effect of in-plane friction. In order to compensate in-plane stress, a pressure was introduced into the two cavities and then was reduced to half its value before the induced charge was measured on dropping the pressure from the intended point to zero. d_{33} of the ferroelectric films can be determined by dividing the pressure-induced charge by the product of the pressure change inside the cavities and the area of the top electrode.

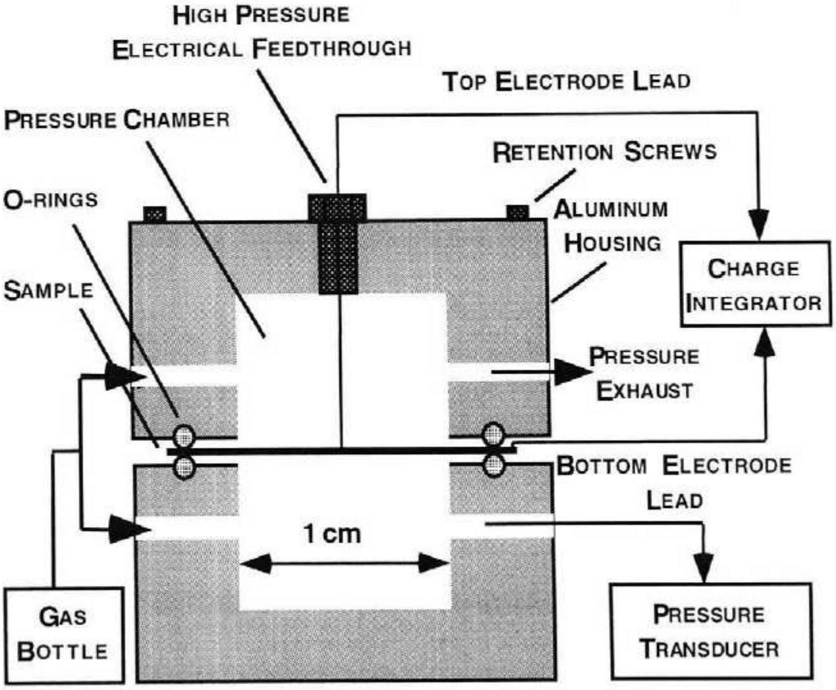

Fig. 3.9 Experimental setup for the d_{33} measurement from Xu [72].

Chapter 4 $LaNiO_3$ Processing-Property Relationships

DC magnetron sputtering was used to deposit $LaNiO_3$ thin films in this work. The effects of deposition parameters on the structure and orientation of the resulting films were investigated using x-ray diffraction. The resistivity of $LaNiO_3$ films was measured as a function of temperature. High temperature structural analyses were conducted and the surface morphology of the films was examined by atomic force microscopy.

4.1 The Effects of Deposition Parameters

Targets of $LaNiO_3$ were fabricated by sintering the powder prepared by a molten salt technique as described in chapter 3. In order to obtain highly (100)-textured $LaNiO_3$ thin films, the effects of deposition parameters were investigated systematically. The working pressure, gas ratio of O_2 and Ar, and substrate temperature are key parameters in the deposition. $LaNiO_3$ thin films were grown on bare silicon and quartz substrates at a power of 200W. The resulting $LaNiO_3$ films were analyzed by x-ray diffraction.

As shown in Fig. 4.1 (a), $LaNiO_3$ films were deposited on bare (native oxide only) silicon substrates at temperatures from 300°C to 700°C and a working pressure of 50 mtorr with a gas ratio of 50%O_2 and 50%Ar. Films deposited at 300°C and 400°C exhibited very weak peaks. This indicated that the films were largely amorphous. While the amorphous films can be crystallized at high temperature after the deposition, it is difficult to control the final orientation in this way. Therefore this is not a suitable approach to obtain textured films. Higher substrate temperatures improve the crystallization of the $LaNiO_3$ films. Films deposited at 500°C exhibited strong (100) orientations and a weak (110) peak. It is difficult to obtain highly (100)-textured $LaNiO_3$ films when depositions were carried out at temperatures greater than 600°C. Films deposited at 600°C and 700°C had weaker (100) peaks and stronger (110) peaks. As substrate temperatures increased, both the adatom mobility and the intensity of (110) peaks increased. This indicated that (100) texture was favored when adatom mobility was low and higher adatom mobility conditions lead to random film orientation. This may be due to a lower surface energy for the densely packed (100) planes relative to the (110) planes. Fig. 4.1 (b) shows the lotgering factor as a function of deposition temperature (See Equation 3.1). It is clear that the degree of (100) orientation decreased for deposition temperatures above 500°C.

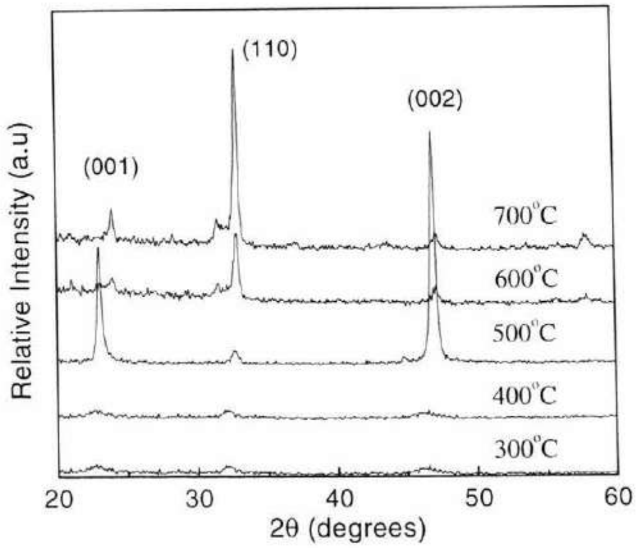

Fig 4.1 (a) XRD patterns of $LaNiO_3$ thin films deposited on Si at different temperatures.

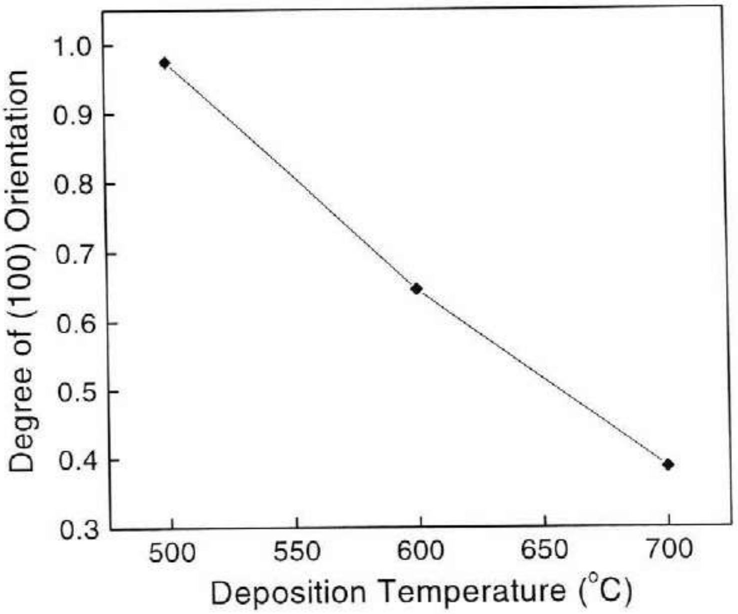

Fig 4.1 (b) Degree of $LaNiO_3$ (100) orientation as a function of deposition temperature.

The effect of gas ratio was also investigated for films prepared at a working pressure of 50 mtorr at 500°C. The XRD patterns and degree of (100) orientation vs. O_2 content are given in Fig. 4.2. It is difficult to obtain both texture and well crystallized films when the films were deposited without O_2. So it is clear that an oxidizing atmosphere is necessary for depositions of textured films. When the content of O_2 was greater than 50%, bombardment of the film's surface by negative ions O_2^- and reflected should increase and the sputtering rate became smaller. This apparently suppressed the growth of (100)-oriented grains and (110)-oriented grains dominated the microstructure. So the $LaNiO_3$ films deposited using Ar/O_2 of 40/60 and 30/70 exhibited strong (110) peaks rather than (100) orientation.

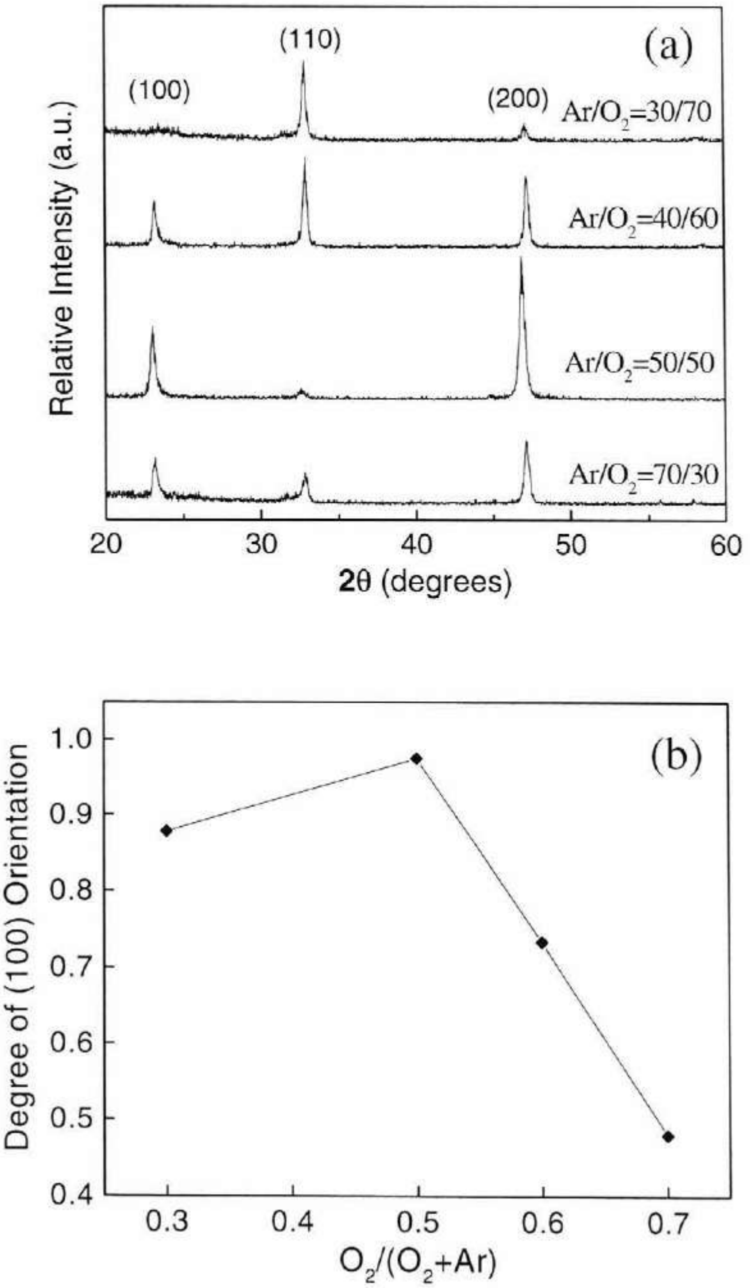

Fig 4.2. (a) XRD patterns of $LaNiO_3$ thin films deposited using different Ar/O_2 ratios, (b) degree of (100) orientation as a function of content of O_2.

The working pressure also affected the growth and texture of $LaNiO_3$ films. As shown in Fig. 4.3, $LaNiO_3$ films were deposited at 500°C with a gas ratio of 50%O_2 and 50%Ar. The degree of (100) orientation increased when the working pressure increased from 20 mtorr to 50 mtorr. When the working pressure increased, the mean free path of gas species decreased and more collisions took place in the gas phase, so the energy of arriving species is lower. So the pressure change decreased the adatom mobility on the film surface. As was suggested by the growth at different temperatures, (100) texture is favored by lower adatom mobility. Thus, a higher working pressure enhanced the (100) orientation. However, it was found that the growth rate decreased with increasing working pressure (~ 460 Å/hour for 20 mtorr, ~ 370 Å/hour for 35 mtorr, 300 Å/hour for 35 mtorr). If the working pressure is too high, the growth rate will be low. It took an excessively long time to obtain a required thickness. Therefore the working pressure should not be too high. The working pressure used here (50 mtorr) lead to growth rate of ~ 300 Å/hour.

To examine the texture of $LaNiO_3$, the rocking curve for the 002 peak was measured for films deposited at different conditions (see Fig. 4.4-4.5). As shown in Fig. 4.4, the full width at half maximuma (FWHM) of different $LaNiO_3$ films changed with the gas ratio of Ar/O_2. The film deposited using an Ar/O_2 of 50/50 had a minimum FWHM of 6.6°. Contents of O_2 either greater than 60% or less than 50% resulted in larger FWHM. This agreed with the XRD patterns shown in Fig. 4.2. The films deposited at 300°C, 400°C and 700°C had very weak 200 peaks. As shown in Fig. 4.5, the films prepared at 600°C exhibited a FWHM of 13.2° which is larger than that of the films deposited at 500°C. The FWHM of different $LaNiO_3$ films are listed in Table 4.1.

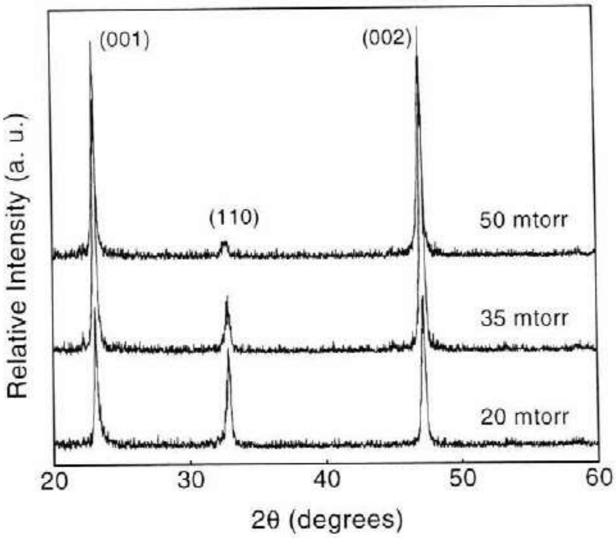

Fig. 4.3 (a) XRD patterns of $LaNiO_3$ thin films deposited on Si under different pressures

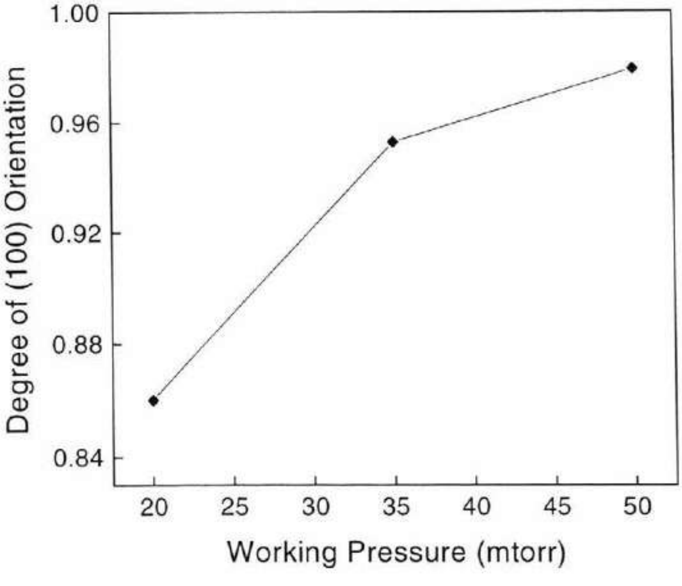

Fig. 4.3 (b) Degree of $LaNiO_3$ (100) orientation as a function of working pressure

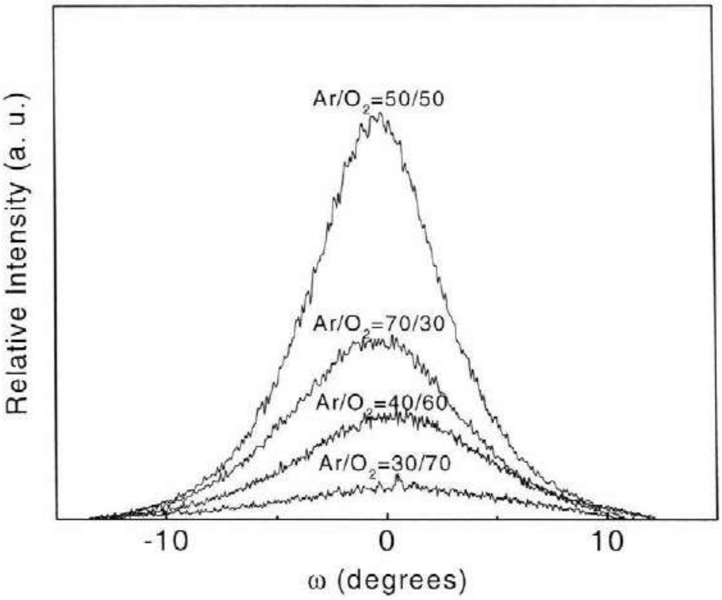

Fig. 4.4 Rocking curves of 200 peak of different $LaNiO_3$ films

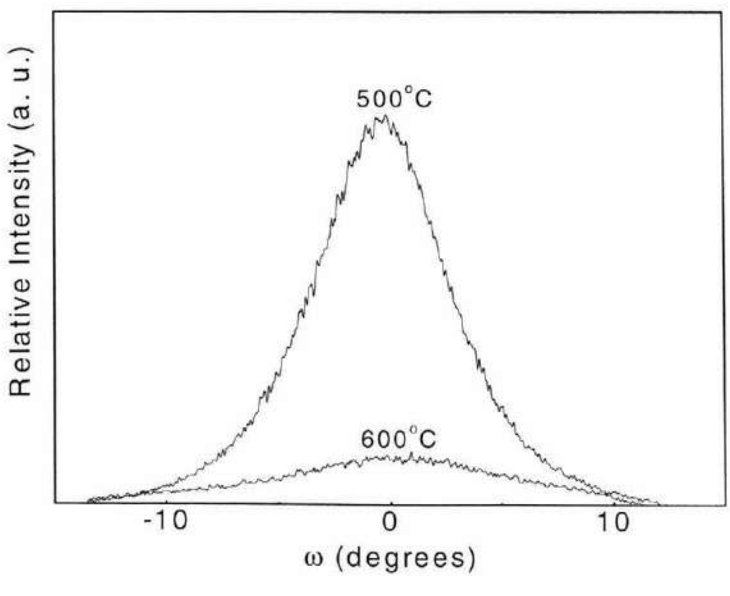

Fig. 4.5 Rocking curves of 200 $LaNiO_3$ peak as a function of temperature

Table 4.1 FWHM of $LaNiO_3$ films deposited at different conditions

T(°C)	Ar/O_2	FWHM(°)
500°C	30/70	12.3
	40/60	9.7
	50/50	6.6
	70/30	8.9
600°C	50/50	13.2

Table 4.2 summarizes optimal processing parameters for depositions of strongly (100) textured $LaNiO_3$ films. Samples deposited under the optimal condition were analyzed using X-ray diffraction (XRD) and atomic force microscopy (AFM). Fig. 4.6 gives the XRD pattern of the highly (100)-textured $LaNiO_3$ thin films. As discussed in chapter 3, the relative intensity of *(00l)* of the $LaNiO_3$ film was calculated to be 97% using the normalized data with respect to randomly textured $LaNiO_3$ in equation 3.1.

Because ferroelectric thin films were deposited onto $LaNiO_3$ films, it is helpful to examine the topography of the $LaNiO_3$ films. Fig. 4.7 gives the AFM image of a (100)-textured $LaNiO_3$ thin film. A rms roughness of ~ 3 nm was measured from line scans across the film surface. A grain size of ~ 0.04 μm was also determined in the image. Compared to the image of the film with random orientation shown in Fig. 4.8, the (100)-textured film with the same thickness had a finer grain size and a rougher surface due to smaller adatom mobility. Its growth rate was also higher. Table 4.3 summarizes the growth rate, grain size and roughness for (100)-textured and random $LaNiO_3$ films.

Table 4.2 Optimized processing parameters for (100) textured $LaNiO_3$ thin films

Temperature	480-500°C
Gas ratio	50%O_2 + 50%Ar
Working pressure	50 mtorr
Power	200 W
Target to substrate distance	11 cm

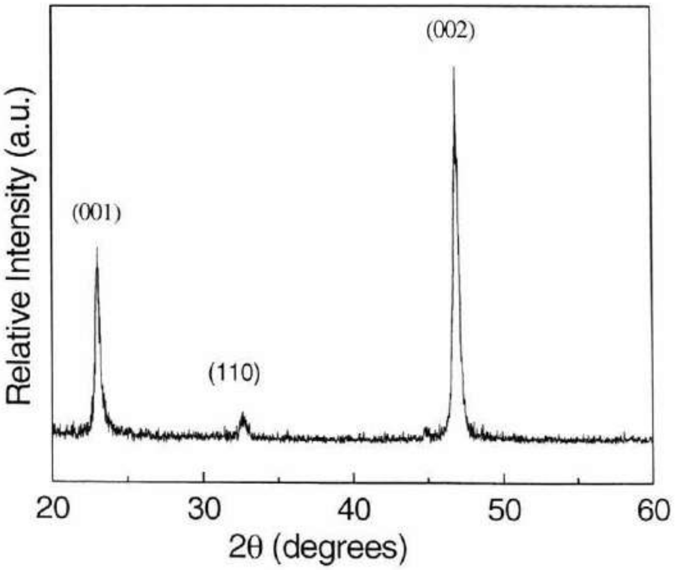

Fig. 4.6 XRD pattern of a $LaNiO_3$ thin film deposited on Si under the optimal conditions.

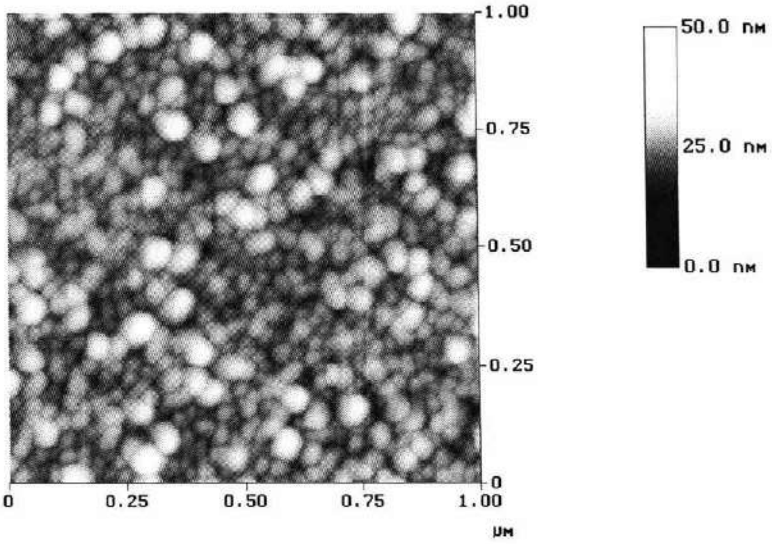

Fig. 4.7 AFM image of $LaNiO_3$ thin films with strong (100) orientation

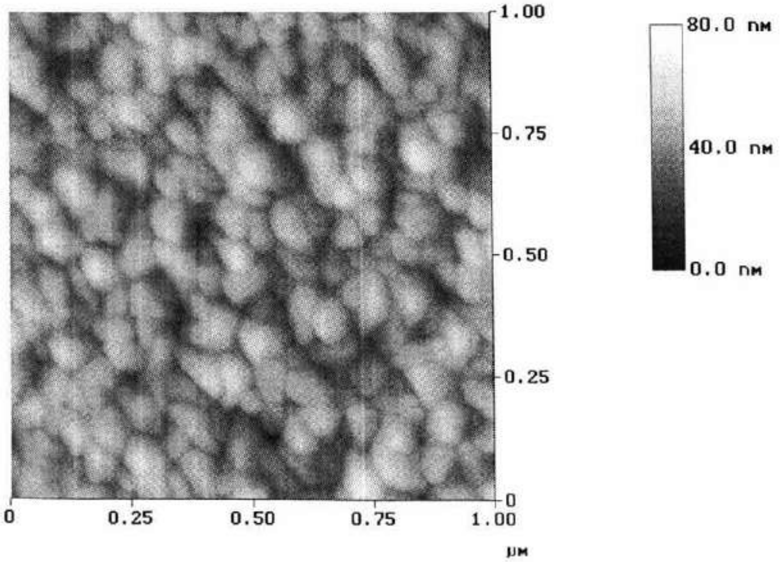

Fig. 4.8 AFM image of $LaNiO_3$ thin films with random orientation

Table 4.3 Comparison of random and (100)-oriented $LaNiO_3$ films

Sample	Growth rate (Å/hr)	Grain size (μm)	Roughness (nm)
random	~180	~0.08	1.6
(100)-oriented	~300	~ 0.04	3

4.2 High Temperature Structural Analyses

In order to better understand the properties of ferroelectric films deposited on $LaNiO_3$ electrodes, it is necessary to consider the lattice mismatch between the ferroelectric layer and $LaNiO_3$. The residual stresses originate from growth strains and thermal strains due to the thermal expansion mismatch [60]. Since residual stress affects the performance of the ferroelectric films by affecting the domain structure [73], an accurate measurement of the thermal expansion coefficient of $LaNiO_3$ films is useful to evaluate the residual stress. Thus, high temperature X-ray diffraction was used to determine the lattice parameter and the thermal expansion coefficient of a (100) oriented $LaNiO_3$ thin film. Only the 200 peak was measured, and the lattice parameter was calculated assuming a pseudocubic cell.

Fig. 4.9 shows that the lattice parameter a_{pc} increased linearly with temperature up to 800°C. A slope change is apparent above that temperature. Two possibilities for the slope change exist. First, the enhanced diffusion at elevated temperatures might cause creep, grain growth or stress relief. Alternatively, Obayashi *et al.* reported the phase transition from a rhombohedrally distorted perovskite to the cubic prototype phase occurred at 940°C in powders [26]. So the phase transition might be another reason for the slope change. If so, then the film transition temperature is about 140°C lower than that of bulk materials. It is not uncommon for structural transitions to occur at lower temperatures in thin films [74]. However, the fact that heating and cooling runs do not retrace at any lower temperatures suggests that stress relief rather than the phase transition accounts for the anomaly in the lattice parameter versus temperature data.

The lattice parameter versus T curves for heating and cooling were approximately parallel below 800°C. The initial lattice parameter of the pseudocubic unit cell for the $LaNiO_3$ thin films is 3.845 ± 0.01 Å at room temperature. This value is slightly extended with respect to the powder data reported in the literature (pseudocubic a = 3.838 Å) [19]. On cooling from 1000°C, the lattice parameter is 3.839 Å, closer to the bulk data, which is consistent with the supposition of strain relief at high temperatures.

A thermal expansion coefficient of $16.3 \times 10^{-6}/^{\circ}C$ was determined at temperatures below 800°C from the lattice parameter versus temperature data. A very similar number was obtained when data were taken below the deposition temperature to minimize the effect of the relaxation. The thermal expansion coefficient is much larger than that of Si substrate ($3.8 \times 10^{-6}/^{\circ}C$) and PMN-PT ($9 \times 10^{-6}/^{\circ}C$). Thus, a large stress will be expected in the layer structure of PMN-PT/$LaNiO_3$/Si after heat treatment due to the thermal expansion mismatches. The thermal strain is proportional to temperature change, so a low annealing temperature is preferred in the preparation of PMN-PT thin films to prevent large stresses.

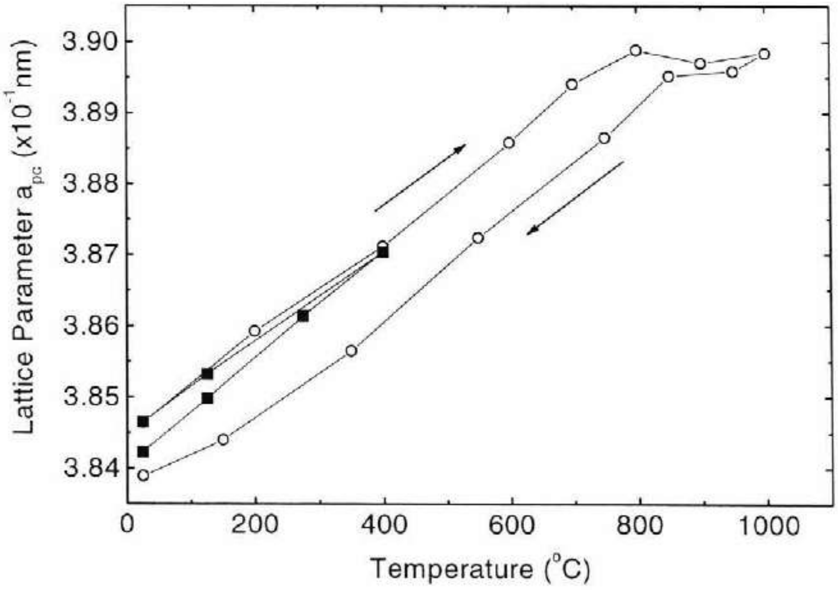

Fig. 4.9 Lattice parameter of $LaNiO_3$ thin films as a function of temperature

4.3 Resistivity of $LaNiO_3$ Thin Films

Since the $LaNiO_3$ thin films are used as bottom electrodes for ferroelectric films, the resistivity of $LaNiO_3$ is important. Thus, a four-point probe was used to measure the resistivity of $LaNiO_3$ films from room temperature to 300°C. Fig.4.9 gives a plot of resistivity as a function of measure temperature for 600 Å thick $LaNiO_3$ film deposited on glass under the optimal conditions (The degree of (100) orientation is 83%). As shown in Fig. 4.10, the resistivity increases with temperature. $LaNiO_3$ thin films exhibited a typical metallic behavior with a resistivity of 8.0×10^{-6} Ω·m at room temperature and a TCR of 0.55%/°C.

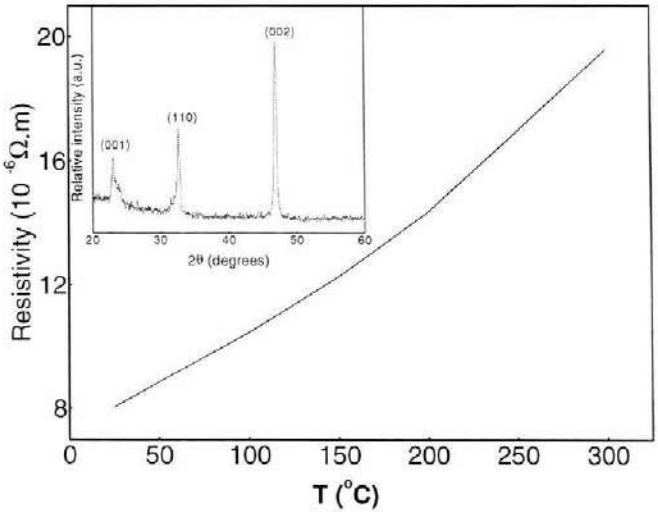

Fig. 4.10 Resistivity as a function of temperature for a 600 Å thick $LaNiO_3$ film on glass. The inset shows the XRD pattern of the film.

The resistivity of thin films can be written as

$$\rho = \rho_{ph} + \rho_g + \rho_s \qquad \text{(equation 4.1)}$$

where ρ_{ph} relates to phonon interaction, ρ_g is the component corresponding to the scattering at geometrical structure defects, and ρ_s corresponds to the surface scattering [75]. ρ_{ph} increases with increasing temperature. At high temperature, ρ_{ph} is the major contributor of resistivity. Grain boundaries, one kind of geometrical structure defects, also contribute to resistivity. A smaller grain size means more grain boundaries and has a stronger scattering, which results in more contributions to the resistivity. A smaller resistivity will be expected on a $LaNiO_3$ sample with a larger grain size. The small grain size of the $LaNiO_3$ films used in this work may account for the comparatively high observed resistivity.

4.4 Summary

Highly (100)-textured $LaNiO_3$ films were grown on silicon and glass substrates. The influence of substrate temperature, gas ratio and working pressure on texture was studied and optimal parameters were determined. The texture of the resultant $LaNiO_3$ films was characterized using X-ray rocking curves. The full width at half maximum (FWHM) of the 200 reflection of these $LaNiO_3$ films is ~ 6.6°.

High temperature structural analyses were performed on $LaNiO_3$ films using high temperature X-ray diffraction. It is found that the films apparently undergo a strain relief at elevated temperatures. A thermal expansion coefficient of $16.3 \times 10^{-6}/^{\circ}C$ was determined at temperatures below $800^{\circ}C$ for $LaNiO_3$ films. The coefficient is much larger than that of Si substrate ($3.8 \times 10^{-6}/^{\circ}C$) and PMN-PT ($9 \times 10^{-6}/^{\circ}C$). The initial lattice parameter of the $LaNiO_3$ thin films is 3.845 Å at room temperature.

The temperature dependence of resistivity of $LaNiO_3$ films was characterized using four-point probe. $LaNiO_3$ thin films exhibited a typical metallic behavior. The resistivity at room temperature was determined to be $8.0\times10^{-6}\ \Omega\cdot m$ for the films.

Chapter 5 PMN-PT Structure and Properties

5.1 Structure and Properties of $PbTiO_3$ and PZT (52/48) Films

To examine the utility of $LaNiO_3$ thin films as bottom electrodes, $PbTiO_3$ thin films were deposited on $LaNiO_3$/Si substrates using 0.2 Molar $PbTiO_3$ solutions. The substrates were spin coated with the $PbTiO_3$ solution at 1500 rpm for 30 seconds, and then heated on a hot plate at 350°C for 150 seconds. The resultant samples were annealed at 650°C for 60 seconds after every four layers. The thickness of each layer was ~ 80nm. Fig. 5.1 presents the X-ray diffraction pattern of a $PbTiO_3$/(100)$LaNiO_3$/Si layer structure with a 0.06μm thick $LaNiO_3$ layer and 0.5μm of $PbTiO_3$. A strong (100) texture was observed for the sol-gel derived $PbTiO_3$ film. However, a random orientation was obtained if $PbTiO_3$ films were coated on randomly oriented $LaNiO_3$ thin films. Thus the orientation of the bottom electrodes dominates the orientation of the $PbTiO_3$ layers. This is encouraging for depositions of other lead-based ferroelectric thin films such as PZT and PMN-PT.

PZT thin films deposited onto Si substrates with highly (100)-textured $LaNiO_3$ bottom electrodes were then investigated. The substrates were spin coated with a PZT (52/48) solution at 1500 rpm for 30 seconds, and then heated on a hot plate at 340°C for 150 seconds. The samples were annealed at 700°C for 60 seconds for each layer (about 0.13μm thick). This is necessary because the samples didn't show strong (100) texture and converged to a random orientation with increasing numbers of layers if they were annealed after every four layers. After deposition, the samples were analyzed using X-ray diffraction. Fig. 5.2 gives the XRD pattern of a 0.5μm thick PZT film coated on a (100)-textured $LaNiO_3$ bottom electrode. Strong (100) texture was obtained for the sol-gel derived PZT film. The PZT (52/48) film exhibited a dielectric constant of 1100 and loss tangent of 4.6%. The d_{31} of the PZT film was determined to be –45pC/N after it was poled under 150kV/cm for 5 minutes.

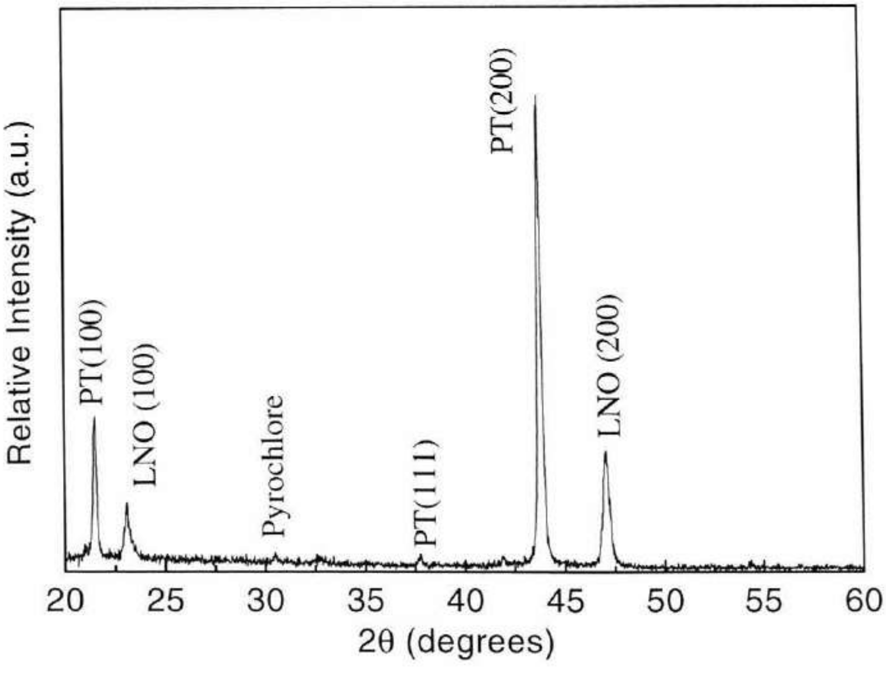

Fig. 5.1 XRD pattern of $PbTiO_3$ films coated on (100)-textured $LaNiO_3/Si$ substrates

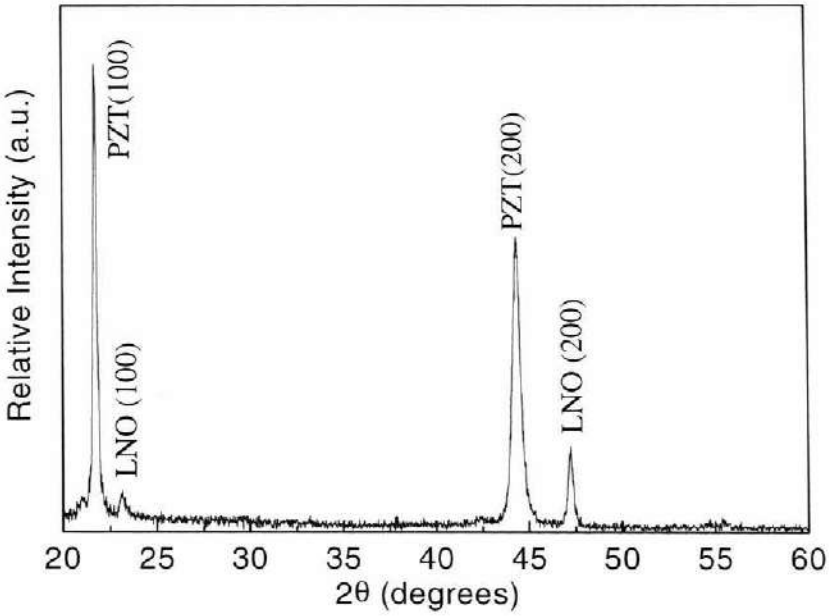

Fig. 5.2 XRD pattern of PZT (52/48) films coated on (100)-textured $LaNiO_3/Si$ substrates

5.2 Deposition of PMN-PT (70/30 and 65/35)

Highly (100)-textured $PbTiO_3$ and PZT (52/48) thin films were deposited successfully onto Si substrates with (100)-textured $LaNiO_3$ bottom electrodes. Deposition of PMN-PT thin films onto the same substrates was the next step of this work. To prepare PMN-PT thin films using the sol-gel technique, the solution was spin coated on substrates at 7500 rpm for 30 seconds. Then PMN-PT layer was pyrolyzed at 360°C for 150 seconds on a hot plate and crystallized at 600-800°C for 60 seconds in a RTA for each layer. The thickness of each layer was about 0.09 μm. PMN-PT adopted a random orientation on $LaNiO_3$ layers that were not highly (100)-textured. The PMN-PT maintained (100)-

orientation on well-oriented (100) $LaNiO_3$ layers when crystallized layer by layer. Otherwise the PMN-PT films converged to a random orientation with increasing numbers of layers, probably as a result of heterogeneous nucleation from the film surface. Using this route, PMN-PT thin films can maintain (100) orientation up to 32 layers (~ 3μm).

As discussed in chapter 4, in order to reduce the residual stress induced by thermal expansion mismatch, a low annealing temperature is desired for the deposition of PMN-PT films. The influence of the annealing temperature on the structure and properties were investigated for PMN-PT thin films. Samples annealed at different temperatures were analyzed using X-ray diffraction. Fig. 5.3 shows XRD patterns of 0.9 μm thick PMN-PT (70/30) films annealed at temperatures of 600, 650, 700 and 750°C. The samples exhibited a high degree of (100) texture and the perovskite phase if they were annealed at 650°C and above. The pyrochlore phase appeared in the sample annealed at 600°C. Use of the $LaNiO_3$ electrode lowers the crystallization temperature for the perovskite phase by ~50°C relative to deposition on Pt-coated Si [58]. This is probably because of the good structure match between the ferroelectric and the perovskite oxide electrode. Thus $LaNiO_3$ electrodes should enable lower residual stresses in (100) PMN-PT films than has previously been reported.

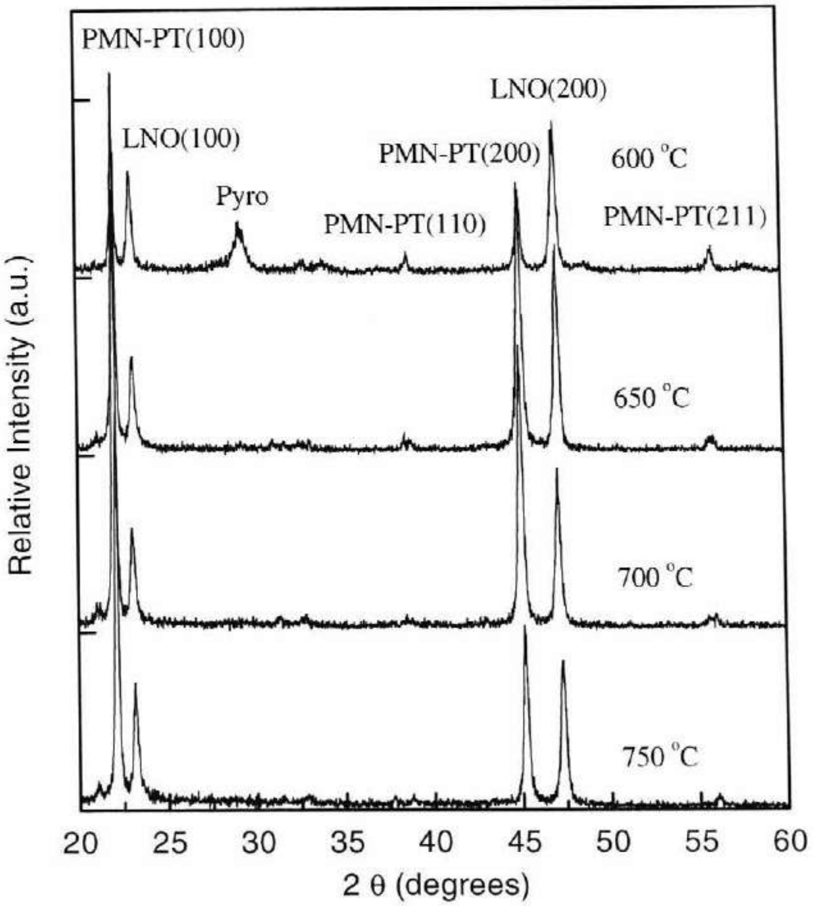

Fig. 5.3 XRD patterns of 0.9μm thick PMN-PT (70/30) films annealed at different temperatures.

The topography of these films was analyzed by AFM to examine the effect of the crystallization temperature on the film morphology. The AFM images are shown in Figs. 5.4 to 5.7. The image scale is 1 μm for all cases. PMN-PT films annealed at 600°C had a smooth surface and revealed an rms roughness value of approximately 0.5 nm. The poor delineation of grain boundaries was probably a consequence of poorer crystallinity than the other films. In addition, previous reports have shown that when pyrochlore is present at the surface of PZT films it has an extremely fine grain structure that is difficult to image [76]. PMN-PT films annealed at 650°C had a rms roughness of approximately 2.8 nm and better developed grain morphologies. The value of the rms roughness continued to increase with annealing temperature. PMN-PT films annealed at 700°C had an rms roughness of approximately 4.2 nm and a larger grain size of ~ 0.1 μm. Films annealed at 750°C had an rms roughness of approximately 6.2 nm and almost the same grain size as those annealed at 700°C.

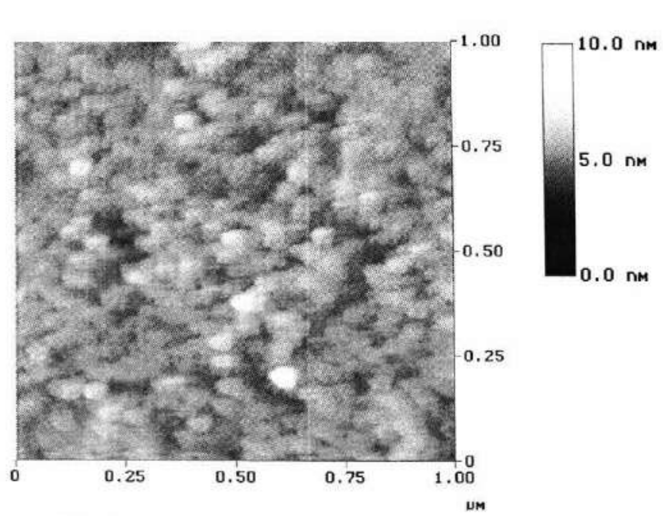

Fig. 5.4 AFM image of 0.9 μm thick PMN-PT (70/30) thin film annealed at 600°C

An X-ray rocking curve was used to examine the texture of a 0.9 μm thick PMN-PT (70/30) thin film annealed at 700°C. Fig. 5.8 gives the rocking curve of the 200 film peak of PMN-PT and $LaNiO_3$. The analysis of the rocking curve revealed the full width at half maximum (FWHM) of the 200 reflection of PMN-PT (70/30) films is almost same as that of $LaNiO_3$ (~ 6.9°).

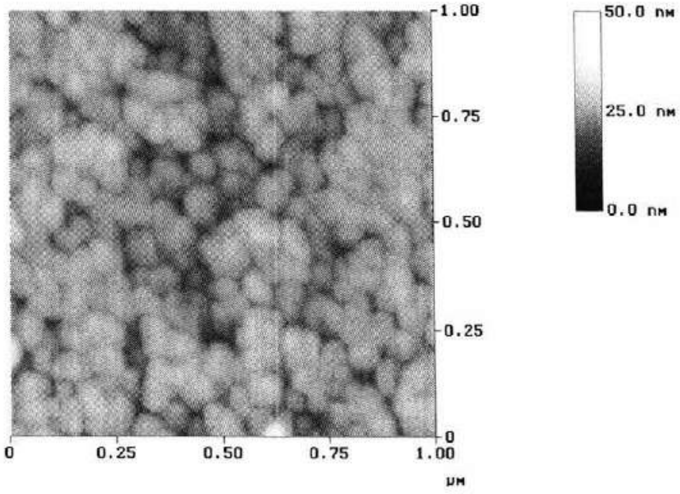

Fig. 5.5 AFM image of 0.9 μm thick PMN-PT (70/30) thin film annealed at 650°C

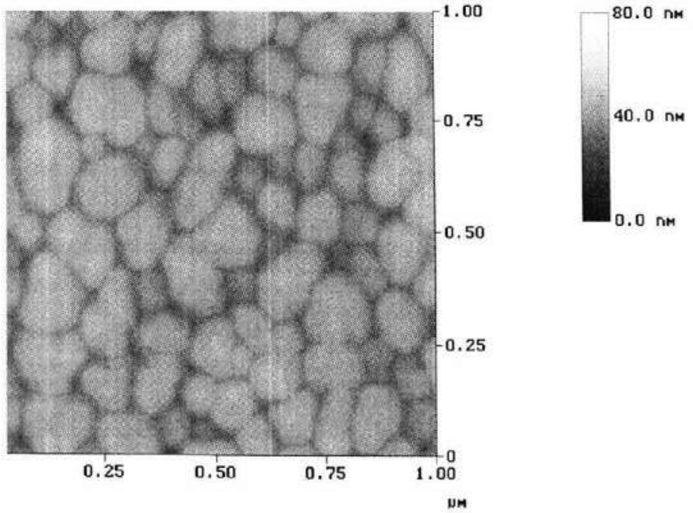

Fig. 5.6 AFM image of 0.9 μm PMN-PT (70/30) thin film annealed at 700°C

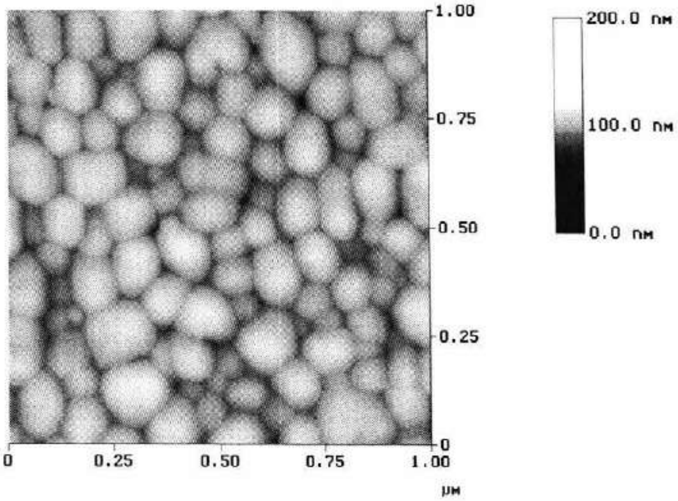

Fig. 5.7 AFM image of 0.9 μm PMN-PT (70/30) thin film annealed at 750°C

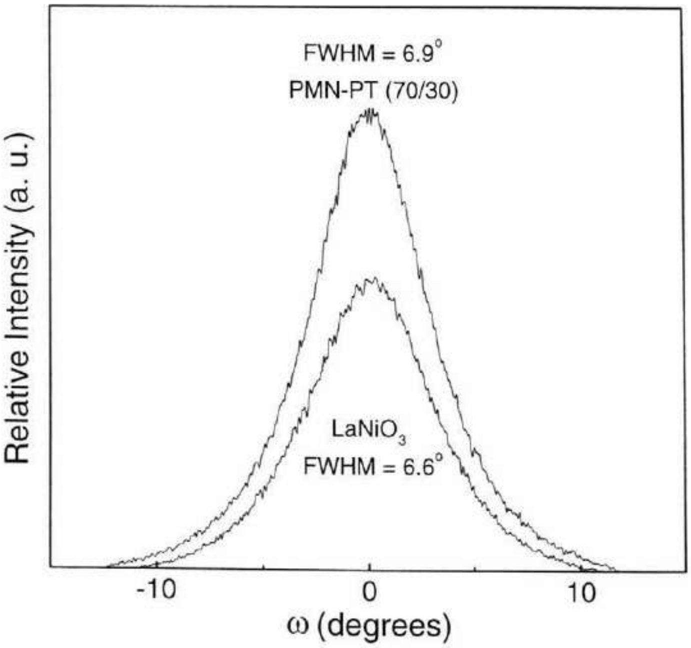

Fig. 5.8 Rocking curve of 200 reflection of a 0.9 μm thick PMN-PT (70/30) film

5.3 Dielectric Properties of PMN-PT

Because the annealing temperature affected the structure of PMN-PT thin films, it also affected the properties of the films. Fig. 5.9 shows dielectric properties as a function of annealing temperature for (001)-textured PMN-PT (70/30, 0.9μm thick) thin films coated on (100)-textured $LaNiO_3/Si$ substrates. As illustrated in Fig. 5.9, the dielectric constant increased with annealing temperatures and reached a maximum at 700°C. One possible reason is that the grain size and crystallinity increased with annealing temperature below 700°C. The room temperature loss tangent was less than 0.07 in all cases. As stated before, a lower annealing temperature is preferred in this work. Since PMN-PT films annealed at 700°C have almost the same structure and better dielectric properties than those crystallized at 750°C, subsequent work focused on PMN-PT films annealed at 700°C.

5.4 Field Dependence of Dielectric Properties

The electric field dependence of the dielectric properties was measured at 1kHz at room temperature for PMN-PT (65/35). Fig. 5.10 gives the tunability of ε_r and $\tan\delta$ as a function of applied electric field up to 120kV/cm for a 1.1μm thick PMN-PT (65/35) film. As observed in Fig. 5.11, the dielectric constant ε_r decreased with increasing electric field and had a 32% change at a field of 50kV/cm. Since the material is ferroelectric, the

ε_r-E curve is hysteretic. The loss tangent as a function of bias voltage had a similar shape to the ε_r curve.

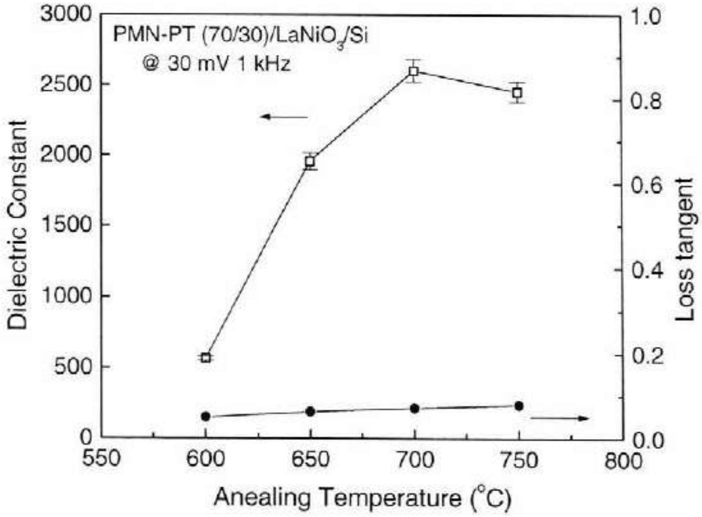

Fig. 5.9 Dielectric properties as a function of annealing temperature for (100)-textured PMN-PT (70/30) thin films.

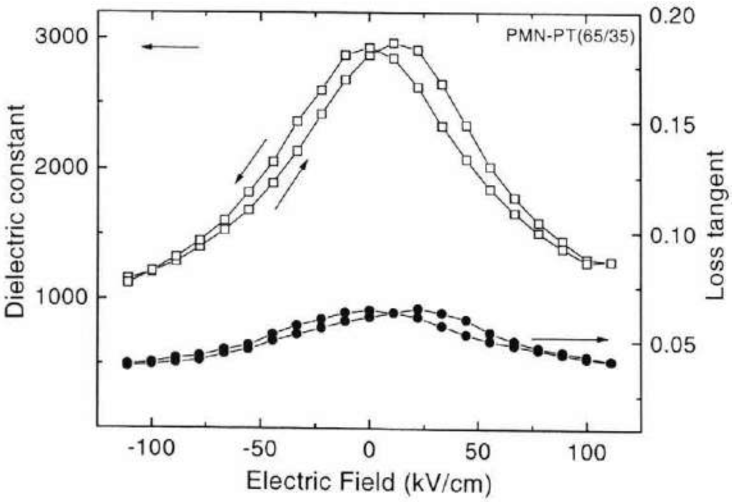

Fig. 5.10 Field dependence of dielectric properties of 1.1 μm thick PMN-PT (65/35).

5.5 Residual Stress in PMN-PT

One source of stress in thin films is the difference in thermal expansion coefficient between the film and the substrate [60]. This is usually the dominant source of stress in sol-gel ferroelectric films, and was assumed to be so in this work as well. The PMN-PT thin films are expected to be in residual tensile stress at room temperature due to the mismatch of thermal expansion of PMN-PT films and Si substrates. It is possible that the residual tensile stresses in the PMN-PT film clamps the domains and makes them difficult to pole through the thickness. This would especially be the case if the stresses were large enough to induce tetragonal material in (001) films. Smaller residual stress is preferred to get large polarization. Therefore, smaller residual stress and larger polarizations would be expected when the annealing temperature was reduced. The thermal residual stress was calculated to be ~ 158 MPa for PMN-PT thin films cooled down from 700°C to room temperature ($\alpha_{si} = 3.8\times10^{-6}/^{o}C$, $\alpha_{PMN\text{-}PT} = 9\times10^{-6}/^{o}C$ [77]). The stresses were calculated assuming a Young's modulus for PMN-PT (70/30) of 45GPa [78]. The final stress may be an over approximation, given that many PMN-PTs have temperature dependent thermal expansion coefficients, as well as having the possibility of twinning below T_c. Even so, it is likely that the film ends up in tensile stress.

To examine the effect of applied stresses on the PMN-PT films, a 1.1 μm thick (001) oriented sample was placed under controlled levels of biaxial stress by flexing them. As presented in Fig. 5.11 and 5.12, samples under applied biaxial compressive or tensile stress exhibited different hysteresis loops at room temperature. With applied compressive stresses, the hysteresis loop rotated counterclockwise, resulting in an increase of ~12% in the remanent polarization.

The 2D clamping in PMN-PT films could lower the symmetry of the paraelectric phase and may change the relative stability of ferroelectric phases, even to the point of stabilizing new ferroelectric phases. According to the phenomenological thermodynamic theory proposed by Pertsev [79], well-oriented or epitaxial ferroelectric films on tensile substrate should exhibit a monotonic variation or a broad maximum in the temperature dependence of permittivity and a change of the Curie temperature. As shown in Fig. 5.14, the PMN-PT (70/30) films annealed at different temperatures displayed different Curie temperatures. But the shift of Curie temperature is not monotonic. All of the PMN-PT (70/30) films annealed at different temperatures showed good convergence of the permittivities measured at different frequencies above the Curie temperature.

Since the thermal residual stress applied on the PMN-PT film was on the order of 160 MPa, it is difficult to obtain a zero net stress on the sample by externally applied stresses. In order to estimate the impact of this large biaxial stress on the remanent polarization (P_r) of the film, a plot of P_r versus stress was extrapolated linearly to zero stress. As shown in Fig. 5.13, the extrapolated P_r was 17 μC/cm^2. This is still lower than that of a <001>-oriented single crystal (23 μC/cm^2 [4]). Additional sources for lowering the P_r value include the lower Curie temperature of the film relative to bulk PMN-PT (110°C vs. 130°C), stress-induced tetragonal phase in the film and size effects (especially interface layers).

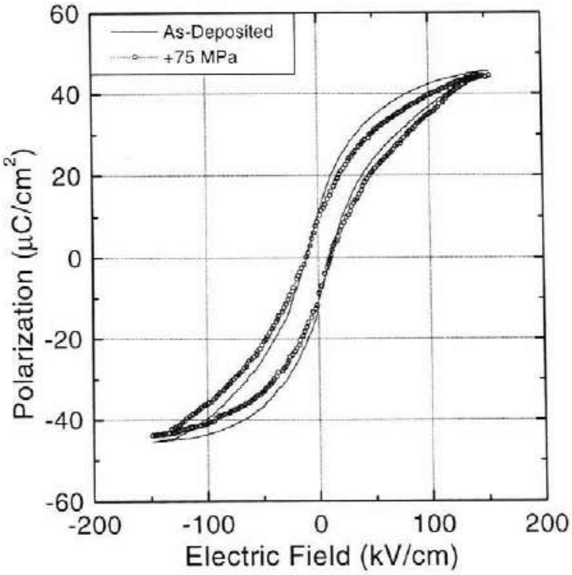

Fig. 5.11 Effect of external biaxial tensile stresses on PMN-PT (70/30) thin film.

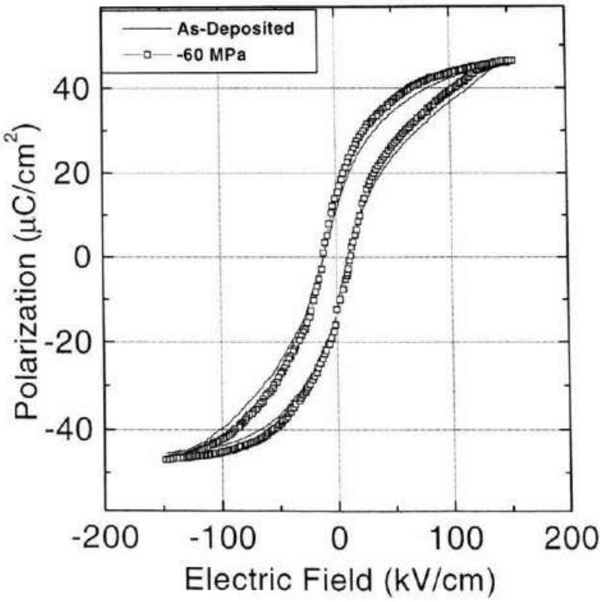

Fig. 5.12 Effect of external biaxial compressive stresses on PMN-PT (70/30) thin film.

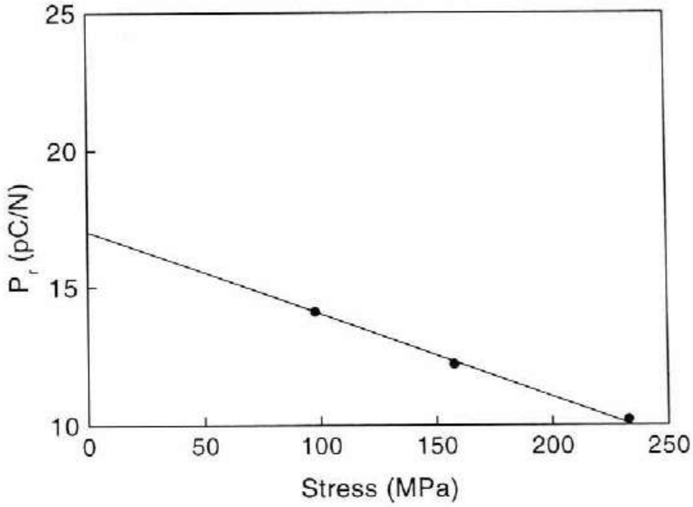

Fig. 5.13 The plot of P_r versus stress for a PMN-PT film coated on $LaNiO_3/Si$

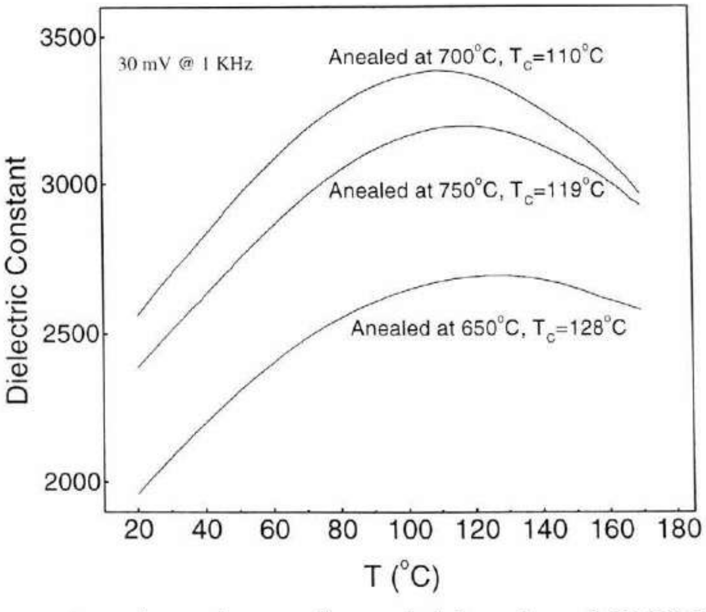

Fig. 5.14 Temperature dependence of permittivity plot of PMN-PT films annealed at different temperatures.

5.6 Piezoelectric Properties of PMN-PT

The effective transverse and longitudinal piezoelectric coefficients (d_{31} and d_{33}) were determined for PMN-PT (70/30) poled under 85kV/cm for 60 minutes. The effective piezoelectric coefficient d_{33} of PMN-PT films was measured using the pneumatic pressure charge method developed by Xu [72]. The effective piezoelectric coefficient d_{33} of a 1.1 μm thick PMN-PT (70/30) film was determined to be ~ 180 pC/N from dividing the pressure-induced charge by the product of the pressure change inside the cavities and the area of the top electrode. The calculated effective piezoelectric coefficient d_{31} of a film depends on the Young's modulus chosen if the wafer flexure technique was used. Effective piezoelectric coefficient d_{31} ~ -79 pC/N was measured for 1.1 μm thick PMN-PT thin films crystallized at 700°C (assuming a Young's modulus of 45GPa). Park *et al.* reported that a d_{33} of 170 to183 pC/N and d_{31} of -64 to -72 pC/N for a 1.2 μm thick (100)-oriented PMN-PT(70/30) films coated on Pt(111)-passivated Si substrates at 750°C [58]. Their values are slightly smaller than those in this work, possibly due to the higher residual stresses resulting from their higher crystallization temperature. The d_{31}/d_{33} ratio of 0.43 is reasonable and indicated that the Young's modulus of (100) PMN-PT (70/30) films is approximately 45GPa.

5.7 Aging of d_{31}

The aging of d_{31} was measured and is shown in Fig. 5.15 for a 1.1 μm thick PMN-PT (70/30) film annealed at 700°C. The film was poled using 85kV/cm for 60 minutes with the top electrode either negative or positive. Aging rates of 6.8%/decade and 3.9%/decade were observed for a sample poled with the top electrode positive and negative, respectively.

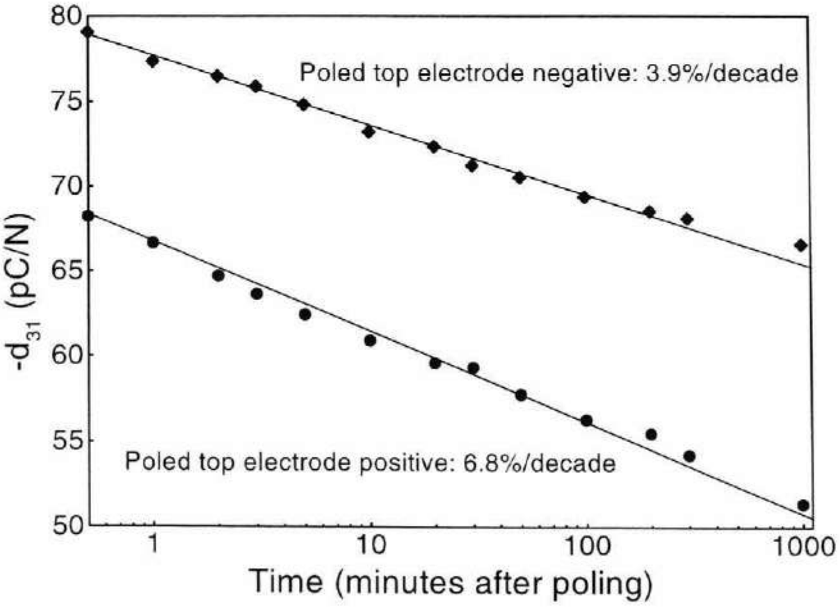

Fig. 5.15 Aging curves of a 1.1 μm thick PMN-PT (70/30) film under different poling conditions

Shepard *et al.* suggested the asymmetries in aging behavior was probably due to an internal electric field. Films poled in directions parallel and antiparallel to the internal bias have modest and larger aging rates, respectively [80]. Since Pt and $LaNiO_3$ layers were used as the top and bottom electrodes for the PMN-PT film, respectively, there is certainly a difference in work functions that could result in an internal electric field. This, in turn, could lead to the asymmetry in aging rates. It would be helpful to confirm this using $LaNiO_3$ for both top and bottom electrodes in the aging measurements. Maria suggested that a large internal bias results in the low aging rate (<1%/decade) of PMN-PT films prepared by pulsed laser deposition [56]. The higher aging rate observed here is consistent with the lack of an obvious shift of the P-E loop along the electric field axis. Polcawich *et al.* demonstrated that either high temperature poling or UV-poling could improve the aging for PZT films [81]. However, when high temperature poling was used here (85 kV/cm for 60 minutes at 80°C), there was very little change in the aging rate.

5.8 Fatigue of PMN-PT Films

The fatigue test was performed using a bipolar square wave of 60kV/cm at 1MHz on a 0.7μm thick PMN-PT (70/30) film with a remanent polarization of 12 $\mu C/cm^2$. As presented in Fig. 5.16, the film with $LaNiO_3$ as the bottom electrode and Pt as the top electrode exhibited very good endurance against fatigue and showed an almost flat profile of the switched charge with negligible decrease in the switched polarization up to 2×10^{10} cycles.

Bornand *et al.* investigated the fatigue behavior of (100) and (111)-oriented $Pb[Yb_{1/2}Nb_{1/2}]O_3$-$PbTiO_3$ (PYbN-PT) thin films coated on $(111)_{pc}$ and $(001)_{pc}$ oriented

$SrRuO_3/(100)_{pc}$-$LaAlO_3$ [4]. They found that the $<001>_{pc}$-growth minimizes the fatigue behavior of relaxor ferroelectric-$PbTiO_3$ materials. Thus, it is possible that the endurance against fatigue in (100)-oriented PMN-PT film is due to (100) orientation. It would be very helpful if a higher P_r film could be grown to confirm this.

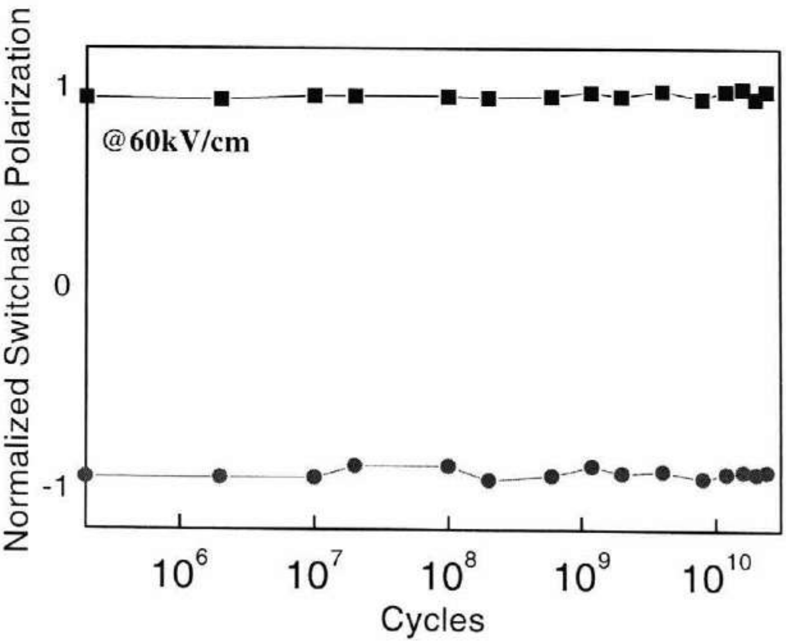

Fig. 5.16 Fatigue behavior of a 0.7 μm thick (100)-oriented PMN-PT (70/30) film. P_r for this sample is 12 μC/cm^2.

5.9 Leakage Current Density

The leakage current density was measured on a 0.6μm thick PMN-PT (70/30) film coated on $LaNiO_3$/Si (see Fig. 5.17). A voltage sweeping from 0 to 11 V was applied to the top electrode for the measurement. Three nearly linear regions were observed for the

PMN-PT films in a log-log plot. The slopes of 1.1, 2.3 and 10.6 were determined for region I, II and III, respectively.

This behavior is quite similar to that which was reported for $PbTiO_3$ films by Fox [82]. In that work, region I (slope = ~ 1) was identified as being a linear Ohmic-like conduction due to thermally induced electrons in the conduction band of the ferroelectric film. The theory of space charge limited conduction proposed by Rose can be used to describe the conduction behavior in the region II (slope = ~ 2) [83]. In this region, the electrodes inject electrons into the PMN-PT films, creating an accumulation region in the PMN-PT films. Defects in the PMN-PT films presumably act as electron traps and absorbed injected electrons. With a sufficiently high voltage was applied, the number of electrons coming from carrier injection became larger than the thermal electrons, resulting the transition from region I to region II. Trap-filled limited behavior was proposed by Lampert *et al.* to explain the behavior in region III (slope = ~ 10.6) [84]. When the voltage applied was increased above the trap-filled limit, all available traps were filled by electrons. Therefore, the carrier injection created an abrupt increase in the number of free electrons, resulting in the transition from region II to region III. As shown in Fig. 5.17, the leakage current density was less than 10^{-6} A/cm^2 in region I (electrical field <100kV/cm). It would be interesting to repeat this experiment with the polarity of the electrodes reversed to examine the difference in injection from Pt and $LaNiO_3$ electrodes.

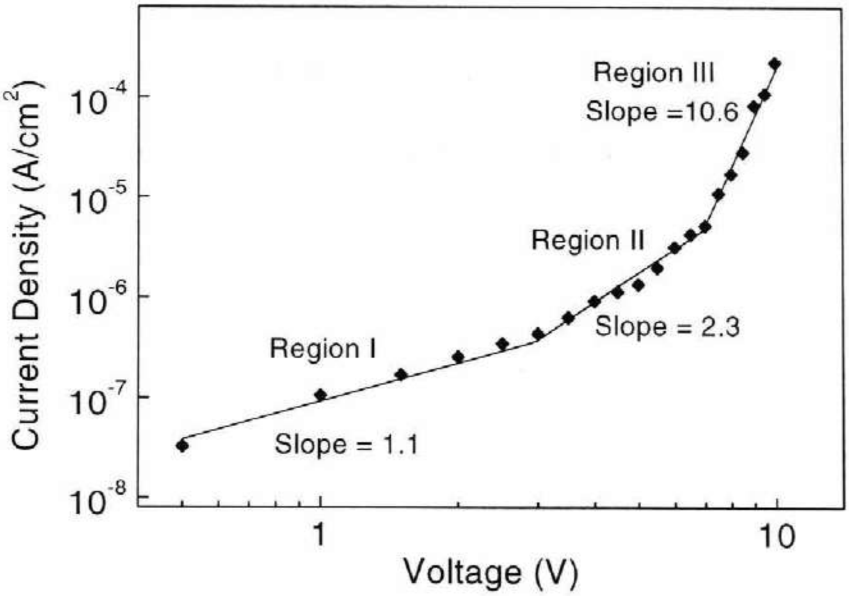

Fig. 5.17 Leakage current density versus applied voltage for a 0.6 μm thick PMN-PT (70/30) films.

5.10 Summary

Strongly (100)-textured $PbTiO_3$ and PZT films were deposited on highly (100)-textured $LaNiO_3$/Si substrates by the sol-gel technique. The PZT (52/48) film demonstrated a dielectric constant of 1100 and loss tangent of 4.6%.

Highly (001)-oriented thin films of PMN-PT (70/30 and 65/35) were also fabricated by a sol-gel method on (100)-textured $LaNiO_3$ metallic oxide electrodes. A remanent polarization of 12 μC/cm^2 was observed for PMN-PT (70/30) films annealed at 700°C. The dielectric constant ε_r decreased with increasing electric field and had a 32% change at a field of 50kV/cm. The loss tangent as a function of bias voltage had a similar shape to the ε_r curve. Effective piezoelectric coefficient d_{33} ~180 pC/N and d_{31} -79 pC/N were measured on 1.1μm thick PMN-PT (70/30) films. Aging rates of 6.8%/decade and 3.9%/decade were observed for the PMN-PT film poled top electrode positive and negative, respectively. A rotation of the hysteresis loop was observed when external stress was applied to the PMN-PT thin films, with compressive stresses leading to higher P_r values and tensile stresses to lower ones. PMN-PT (70/30) films with $LaNiO_3$ bottom electrodes and Pt top electrodes exhibited very good endurance against fatigue. The film showed an almost flat profile with negligible decrease of switching polarization up to 2×10^{10} cycles when a bipolar wave applied an electric field of 60 kV/cm to the film.

Chapter 6 Conclusions and Future Work

6.1 Conclusions

6.1.1 Growth of $LaNiO_3$ thin films

$LaNiO_3$ powder was fabricated for preparation of three-inch targets using a molten salt technique. $LaNiO_3$ films were then grown on silicon and glass substrates by DC magnetron sputtering. The influence of substrate temperature, gas ratio and working pressure on texture was studied and explained by adatom mobility and resputtering mechanisms. Optimal parameters for highly (100)-textured films were determined.

The structure was analyzed using X-ray diffraction. The texture of highly (100)-oriented $LaNiO_3$ films was characterized using X-ray rocking scans. The full width at half maximum (FWHM) of the 200 reflection of $LaNiO_3$ films is 6.6°.

High temperature structural analyses were performed on $LaNiO_3$ films using high temperature X-ray diffraction. A thermal expansion coefficient of $16.3 \times 10^{-6}/^\circ C$ was determined at temperatures below 800°C for $LaNiO_3$ films. The coefficient is much larger than that of Si substrate ($3.8 \times 10^{-6}/^\circ C$) and PMN-PT ($9 \times 10^{-6}/^\circ C$) [77]. The initial pseudocubic lattice parameter a_{pc} of $LaNiO_3$ thin films is 3.845 Å at room temperature.

The temperature dependence of resistivity of $LaNiO_3$ films was characterized using four-point probe. $LaNiO_3$ thin films exhibited a typical metallic behavior. The resistivity at room temperature was determined to be $8.0\times10^{-6}\ \Omega\cdot m$ for the $LaNiO_3$ film. This comparatively high resistivity may be due to scattering from structural defects such as surfaces and grain boundaries. A larger grain size means fewer grain boundaries and lower scattering, which results in smaller resistivity. So a smaller resistivity should be expected in a $LaNiO_3$ sample with a larger grain size.

As shown in Table 6.1, compared to Pt or Pt-based electrodes, $LaNiO_3$ electrodes preferred (100) rather (111) orientation on flat surfaces and were relatively easy to etch. The (100) orientation is critical to developing higher piezoelectric coefficients and better resistance to fatigue. In addition, the electrodes had good adhesion to the silicon substrates. The disadvantages of $LaNiO_3$ electrodes include relatively higher resistivity and higher leakage currents of ferroelectric films with $LaNiO_3$ electrodes.

Table 6.1 Comparison of $LaNiO_3$ and Pt electrodes

	$LaNiO_3$	Pt
orientation	(100)	(111)
resistivity ($\Omega\cdot$m)	$\sim 8 \times 10^{-6}$	1.06×10^{-7} [85]
etching	easy (by HCl + HF)	difficult (by HCl or HNO_3)
adhesion to Si	good	not good

6.1.2 Deposition of Ferroelectric Films on $LaNiO_3$

Strongly (100)-textured $PbTiO_3$ and PZT films were deposited on highly (100)-textured $LaNiO_3$/Si substrates by a sol-gel technique. The PZT (52/48) film demonstrated a dielectric constant of 1100 and loss tangent of 4.6%.

Highly (100)-oriented thin films of PMN-PT (70/30 and 65/35) were also fabricated by a sol-gel method on (001)-textured $LaNiO_3$ electrodes. Although the annealing temperature of the PMN-PT films on $LaNiO_3$ electrodes was reduced to 700°C (which is 50°C lower than that used on Pt electrodes), the PMN-PT/$LaNiO_3$ films still exhibited better dielectric and piezoelectric properties than the PMN-PT/Pt films. A remanent polarization of 12 $\mu C/cm^2$ was observed for (100)-oriented PMN-PT(70/30)/$LaNiO_3$ films annealed at 700°C. Effective piezoelectric coefficients of d_{33} ~180 pC/N and d_{31} -79 pC/N were measured on a 1.1μm thick PMN-PT (70/30) film. Aging rates of 6.8%/decade and 3.9%/decade were observed for PMN-PT (70/30) films poled with the top electrode positive and negative, respectively.

The field dependence of the dielectric properties was studied for PMN-PT (65/35) films. It was found that the dielectric constant decreased with increasing electric field and changed 32% at a field of 50kV/cm. The loss tangent as a function of bias voltage had a similar shape to the ε_r curve.

The influence of external stress was also investigated for PMN-PT (70/30) films. Samples under applied biaxial compressive or tensile stresses exhibited different hysteresis loops at room temperature. A rotation of the hysteresis loop was observed when external stresses were applied to the PMN-PT films. With applied compressive stresses, the hysteresis loop rotated counterclockwise, resulting in an increase in the remanent polarization.

(100)-oriented PMN-PT (70/30) films with $LaNiO_3$ as bottom electrodes and Pt as top electrodes exhibited very good endurance against fatigue, which may be due to its (100) orientation. The PMN-PT films exhibited an almost flat profile with negligible decrease of switching polarization up to 2×10^{10} cycles when a bipolar wave applied an electric field of 60kV/cm on the film.

6.2 Future Work

Potential future work directions consist of the following: attempts to understand the orientation mechanism, deposition of epitaxial PMN-PT films on (100) $LaNiO_3$ films, study of PMN-PT films with different compositions, and use of buffer layers to reduce the residual stress.

Understanding of the orientation mechanism during thin film deposition in physical vapor deposition may help to obtain a desired microstructure and film orientation. The orientation-selection may happen in either the nucleation stage or the grain growth stage. To differentiate these two arguments, films deposited using different deposition times need to be examined by XRD and SEM. If grain growth is orientation-selective, it will be helpful to find out how the species in the plasma affect the film orientation. Ne gas, rather than Ar, could be used in depositions to see the impact on ion bombardment, the deposition rate, the film orientation, and the surface morphology. The angles of ion bombardment could also contribute to the film orientation. Different angles between the substrates and targets can be used in film depositions. More information such as the degree of orientation dependence of the angle and surface morphology will be obtained if depositions are carried out with different ion bombardment angles.

Textured PMN-PT films were fabricated successfully using sol-gel technique. But compared to textured PMN-PT films on Si, epitaxial PMN-PT films on $LaAlO_3$ prepared by pulsed laser deposition exhibit much better piezoelectric properties [52]. It would be very helpful to perform a series of experiments that would enable the relative importance of epitaxy vs. texture to be distinguished from different stress states on the different substrates. Thus, oriented films on $LaAlO_3$ and epitaxial films on Si should be pursued to compare with the existing data.

A study of PMN-PT films with different compositions still remains to be completed. These studies may offer further insight to the relations among composition, structure, and properties. A study of the grain size effect on ferroelectric and piezoelectric properties and the field dependence of piezoelectric properties is likely to help elucidate the domain structure and domain motion contribution to properties.

The ferroelectric properties could be deteriorated by residual stress induced from thermal expansion mismatch. One approach to ameliorate this is to reduce the crystallization temperature of ferroelectric films. But the crystallization temperature can only be reduced to temperatures which can guarantee a good crystallization. To reduce the stresses applied on the ferroelectric films, another possible approach is to use a thick buffer layer (> 0.2 μm) with a thermal expansion coefficient in between the coefficients of Si and ferroelectric films. One candidate would be $KTaO_3$ ($\alpha = 8 \times 10^{-6}/°C$, a = 3.988 Å). Since $LaNiO_3$ can adopt (100) orientation on flat surfaces, $KTaO_3$ can be randomly oriented or even amorphous. A deposition technique with a high growth rate for the $KTaO_3$ layers has to be used to prepare this layer.

References

1. P. K. Larsen, R. Cuppen, and G. A. Spierings, Ferroelectrics, 128, 265 (1992).
2. J. F. Scott and C.A.P. de Araujo, Science, 246, 1400 (1989).
3. Seung-Eek Park and Thomas R. Shrout, J. Appl. Phys., 82, 1804-1811 (1997).
4. V. Bornand, S. Trolier-McKinstry, K. Takemura and C. A. Randall, J. Appl. Phys., 87, 3965 (2000).
5. Seshu B. Desu, Dilip P. Vijay, X. Zhang, BaoPing He, Appl. Phys. Lett., 69, 1719 (1996).
6. G. J. Norga, Laura Fe, D. J. Wouters, and H. E. Maes, Appl. Phys. Lett., 76, 1318 (2000).
7. C. M. Foster, G.-R. Bai, R. Csencsits, J. Vetrone and R. Jammy, J. Appl. Phys., 81, 2349 (1997).
8. R. Ramesh, H. Gilchrist, T. Sands, V. G. Keramidas, R. Hakenaasen and D. K. Fork, Appl. Phys. Lett., 63, 3592 (1993)
9. M. J. Shyu, T. J. Hong, T. J. Yang and T. B. Wu, Jpn. J. Appl. Phys., 34, 3647 (1995).
10. Q. X. Jia, X. D. Wu, G. Song and S. R. Foltyn, J. Vac. Sci. Technol., A 14, 1107 (1996).
11. Ray-Hua Horng, Dong-Sing Wuu, Shih-Hsiung Chan, Ming-Chung Chiang, Tiao-Yuan Huang and Simon Min Sze, Jpn. J. Appl. Phys., Part 1, 37, 885 (1998).

12. Junji Senzaki, Koji Kurihara, Naoki Nomura, Osamu Mitsunaga, Yoshitaka Iwasaki, and Tomo Ueno, Jpn. J. Appl. Phys., Part 1, 37, 5150 (1998).

13. K. P. Rajeev, G. V. Shivakumar and A. K. Raychaudhuri, Solid State Commun., 79, 591 (1991).

14. K. M. Satyalakshmi, R. M. Mallya, K. V. Ramanathan, X. D. Wu, B. Brainard, D. C. Gautier, N. Y. Vasanthacharya and M. S. Hedge, Appl. Phys. Lett., 62, 1233 (1993).

15. H. Ichinose, Y. Shiwa and M. Nagano, Jpn. J. Appl. Phys., 199, 5903 (1994).

16. C. C. Yang, M. S. Chen, T. J. Hong, C. M. Wu and T. B. Wu, Appl. Phys. Lett., 66, 2643 (1995).

17. H. Ichinose, M. Nagano, H. Katsuki and H. J. Takagi, J. Mater. Sci., 29, 5115 (1994).

18. C. R. Cho and D. A. Payne, Appl. Phys. Lett., 71, 3013 (1997).

19. A. Wold, B. Post and E. Banks, J. Amer. Chem. Soc., 70, 4911 (1957).

20. V. M. Goldschmidt, Shrifter Norske Videnskaps-Akad. Oslo 1: Matemot. Naturuid. Klasse, No. 2, (1926).

21. R. D. Shannon, Acta Cryst., A32, 751 (1976).

22. T. R. Shrout, and A. Halliyal, Am. Ceram. Soc. Bull., 66, 704 (1987).

23. L. Pauling, "The Nature of Chemical Bonds", Cornell University, New York (1960).

24. W. C. Koehler and E. O. Wollan, J. Phys. Chem. Solids, 2, 100 (1957).

25. A. Word, R. J. Arnott and J. B. Goodenough, J. Appl. Phys., 29, 387 (1957).

26. Hidehito Obayashi and Tetsuichi Kudo, Jpn. J. Appl. Phys., 14, 330 (1975).

27. M. Sagoi, T. Kinno, T. Hushimoto, J. Yoshida and K. Mizushima, Appl. Phys. Lett., 62,1833 (1993).

28. H. Ichinose, Y. Shiwa and M. Nagano, Jpn. J. Appl. Phys., 199, 5907 (1994).

29. T. F. Tseng, C. C. Yang, K. S. Liu, J. M. Wu, T. B. Wu and I. N. Lin, Jpn. J. Appl. Phys., 35, 4743 (1996).

30. D. L. Smith, Thin Film Deposition: Principles and Practice, McGraw-Hill, Inc. (1995).

31. B. A. Movchan and A. V. Demchishin, Fiz. Metal. Metalloved., 28, 653 (1969).

32. J. A. Thornton, J. Vac. Sci. Technol., 11, 666 (1974).

33. R. Messier, A. P. Giri and R. A. Roy, J. Vac. Sci. Technol., A 2, 500 (1984).

34. C. V. Thampson, Mat. Res. Soc. Symp. Proc., 280, 307 (1993).

35. L. S. Yu, J. M. E. Harper, J. J. Cuomo, and David A. Smith, Appl. Phys. Lett., 60, 4160 (1986).

36. D. J. Kester and R. Messier, J. Mater. Res., 8, 1938 (1993).

37. Y.H. Xu, Ferroelectric Materials, Wiley, New York (1990).

38. S. L. Swartz and V. E. Wood, Condensed Matter News, 1(5), 4 (1992).

39. G. A. Smolenskii, A. I. Agranovskaya, V. A. Isupov, and S. N. Popov, Sov. Phys. Solid State, 2, 2584 (1961).

40. F. Jona, and G. Shirane, Ferroelectric Crystals, Pergamon Press, New York (1962).

41. P. W. Forsbergh, Jr., Piezoelectricity, Electrostriction and Ferroelectricity, Handbuch der Physik, 17, 264, Springer-Verlag, Berlin (1956).

42. W.G. Cady, Piezoelectricity: An Introduction to the Theory and Applications of Electromechanical Phenomena in Crystals, Dover Publications, New York (1946).

43. Z.-Y. Cheng, R. S. Katiyar, X. Yao and A. S. Bhalla, Phys. Rev. B, 57, 8166 (1998).

44. Weilie Zhong, Physics of Ferroelectrics, Scientific Press, Beijing, China (1996).

45. N. Setter and L. E. Cross, J. Appl. Phys., 51, 4356 (1980).

46. C. G. F. Stenger, F.L. Scholten, and A. J. Burggraaf, Solid State Comm., 32, 989 (1979).

47. H. Ouchi, J. Amer. Ceram. Soc., 51, 169 (1968).

48. S. Nomura, T. Takahashi, and Y. Yokomizo, J. Phys. Soc. Japan, 27, 262 (1969).

49. Jin-Soo Kim, So-Jung Kim, Ho-Gi Kim, Duck-Chool Lee, Jpn. J. Appl. Phys., Part 1 38, 1433 (1999).

50. S. W. Choi, T. R. Shrout, S. J. Jang, and A. Bhalla, Ferroelectrics, 100, 29 (1989).

51. M. C. Jiang, T. B. Wu, and J. M. Wu, Mater. Chem. Phys., 38, 369 (1994).

52. Y. Takeshima, K. Shiratsuyu, H. Takagi and K. Tomono, Jpn. J. Appl. Phys. Part 1, 34, 5083 (1995).

53. G. R. Bai, S. K. Streiffer, P. K. Baumann, O. Auciello, Appl. Phys. Lett., 76, 3106 (2000).

54. S. Stemmer, G. R. Bai, N. D. Browning, S. K. Streiffer, J. Appl. Phys., 87, 3526 (2000).

55. M. Tyunina, J. Levoska, A. Sternberg, and S. Leppävuori, J. App. Phys., 86, 5179 (1999).

56. J.-P. Maria, W. Hackenberger, and S. Trolier-McKinstry, J. Appl. Phys., 84, 5147 (1998).

57. K. R. Udayakumar, J. Chen, P. J. Schuele, L. E. Cross, V. Kumar, and S. B. Krupanidhi, Appl. Phys. Lett., 60, 1187 (1992).

58. J. H. Park, F. Xu, and S. Trolier-McKinstry, accepted by J. Appl. Phys.

59. B. Jaffe, W. R. Cook Jr., and H. Jaffe, Piezoelectric Ceramics, Academic Press (1971).

60. S. B. Desu, J. Electrochem. Soc., 140, 2981 (1993).

61. H. H. A. Krueger, J. Acoust. Soc. Am., 43, 576 (1967).

62. R. Y. Nishi, J. Acoust. Soc. Am., 40, 486 (1966).

63. Q. M. Zhang, J. Zhao, K. Uchino, and J. Zheng, J. Mater. Res., 12, 226 (1997).

64. R. F. Brown, and G. W. McMahon, Can. J. Phys., 40, 672 (1962).

65. H. H. A. Krueger, J. Acoust. Soc. Am., 42, 636 (1967).

66. J. F. Shepard Jr., Ph.D. Thesis, The Pennsylvania State University (1998).

67. K. D. Budd, S. K. Dey, and D. A. Payne, Brit. Ceram. Proc., 36, 107 (1985).

68. J. H. Park, D. H. Kang, and K. H. Yoon, J. Am. Ceram. Soc., 82, 2116 (1999).

69. F. Chu, F. Xu, J. Shepard Jr., and S. McKinstry, Mat. Res. Soc. Symp. Proc., 493, 409 (1998).

70. D. J. Green, Introduction to Mechanical Properties of Ceramics, Cambridge University Press (1998).

71. J.-P. Maria, Ph.D. Thesis, The Pennsylvania State University (1998).

72. F. Xu, Ph.D. Thesis, The Pennsylvania State University (1999).

73. B. A. Rotenberg, Soviet Physics Solid State, 1, 1627 (1960).

74. B. Qu, W. Zhong, and P. Zhang, Phys. Rev. B, 52, 766 (1995).

75. L. Eckertova, Physics of Thin Films, Plenum Press (1986).

76. L. A. Bursill, I. M. Reaney, D. P. Vijay, S. B. Desu, J. Appl. Phys., 75, 1521 (1994).

77. S. J. Jang, Ph.D. Thesis, The Pennsylvania State University (1979).

78. S.-E. Park and T. R. Shrout, IEEE Trans. Ultras. Ferroelectric and Freq. Cont., 44 (5), 24 (1997).

79. J. Grindlay, An Introduction to the Phenomenological Theory of Ferroelectricity, Pergamon Press, Oxford (1970).

80. J. F. Shepard Jr., F. Chu, I. Kanno and S. Trolier-McKinstry, J. Appl. Phys., 85, 6711 (1999).

81. R. Polcawich, M.S. Thesis, The Pennsylvania State University (1999).

82. G. R. Fox, Ph.D. Thesis, The Pennsylvania State University (1992).

83. A. Rose, Phys. Rev., 97, 1538 (1955).

84. M. A. Lampert, Phys. Rev., 103, 1648 (1956).

85. W. D. Callister Jr., Materials Science and Engineering: An Introduction, John Wiley and Sons, Inc. (1999).